



POLITECNICO DI TORINO

DEPARTMENT OF MECHANICAL AND AEROSPACE ENGINEERING

Master degree course in Ingegneria Meccanica

A.Y. 2020/2021

Master Degree Thesis

# Thermo magnetic FEM modeling of a PMS motor using experimental data

**Supervisors**

Prof. Aurelio Somà  
Prof. Francesco Mocera

**Candidate**

Stefano VENUTI  
matricola: 270417

OCTOBER 2021

## **Abstract**

Nowadays, the requirements to reduce greenhouse gas emissions and to provide a healthy and more habitable environment, has led to the development of several sustainable alternative for an eco-mobility. Since the improvement of internal combustion engine has reached a steady state point in terms of overall efficiency, the increasingly stringent requirement imposed by international normative standards leading automotive companies to find other alternatives to reduce pollution. Thanks to the exponentially growth of the power electronics, the huge interest on research of high energy and power density batteries and the more integration of the embedded systems, the central role of the electric drive has taken over on the most vehicle applications. The wide use of permanent magnets synchronous motors for electric vehicle application has rapidly spread out, thanks to their capability to provide high torque and efficiency with low weight and size. Since the natural behavior of permanent magnets to demagnetize under severe conditions, both coupled thermal and magnetic, the necessity to understand and predict the phenomena is mandatory. This paper carries out the performance analysis in duty cycle, through real CAN and GPS readings in relevant pathway, with discussion of numerical and graphic technical evaluations. Finite element software has also been used for electromagnetic and thermal calculation in order to set the working point of the magnets and to establish the temperature distribution in the motor itself during the whole thermal transient. A particular overview on the dependence of material used and different cooling solutions adopted is done.

# Contents

List of Figures	IV
List of Tables	VI
<b>1 Introduction</b>	<b>1</b>
<b>2 Model of PM synchronous motor</b>	<b>5</b>
2.1 Brief history of electric machines . . . . .	5
2.2 Types of motors . . . . .	6
2.2.1 DC motors . . . . .	6
2.2.2 AC motors . . . . .	6
2.3 Hybrid vehicles . . . . .	8
2.4 Full electric vehicles . . . . .	10
2.5 Working principles . . . . .	11
2.6 Magnetic theory reminders . . . . .	12
2.7 Computational electromagnetics . . . . .	13
2.8 Electrical model . . . . .	14
2.8.1 Direct and quadrature axis . . . . .	16
2.8.2 Torque production . . . . .	19
2.9 Motor constant . . . . .	20
2.9.1 Back EMF constant . . . . .	20
2.9.2 Torque constant . . . . .	21
2.9.3 Motor constant . . . . .	21
<b>3 Motor design</b>	<b>23</b>
3.1 Electro-magnetic target specification . . . . .	23
3.2 Stator design . . . . .	24
3.3 Electromagnetic analysis of definitive motor configuration . . . . .	28
3.3.1 Brief discussion about attempts done before reaching the final configuration . . . . .	28
3.3.2 Guidining lines for motor design . . . . .	29
3.4 Convergence analysis . . . . .	34
<b>4 Comparative analysis of materials</b>	<b>37</b>
4.1 Stator lamination material . . . . .	38
4.2 Rotor material . . . . .	39

<b>5</b>	<b>Electronic acquisition system for telemetry data</b>	<b>41</b>
5.1	Telemetry data monitoring system . . . . .	41
5.2	Duty cycle definition . . . . .	46
5.3	Post processing data analysis . . . . .	50
5.4	Duty cycle simulation . . . . .	54
5.5	Mechanical stress analysis . . . . .	58
<b>6</b>	<b>Thermal design of a PMSM</b>	<b>61</b>
6.1	General overview . . . . .	61
6.2	Housing water jacket design . . . . .	62
6.3	Duty cycle thermal simulation . . . . .	63
6.4	Demagnetization analysis . . . . .	67
6.5	Thermal design review . . . . .	70
<b>7</b>	<b>Conclusions</b>	<b>73</b>

# List of Figures

1.0.1 Industry 4.0 contents . . . . .	2
2.2.1 Working principle of a DC motor [3] . . . . .	6
2.2.2 AC synchronous motor [5] . . . . .	7
2.2.3 Synchronous reluctance motor [8] . . . . .	8
2.3.1 Parallel hybrid logic . . . . .	9
2.3.2 Series hybrid logic . . . . .	9
2.4.1 Logic box of a BEV . . . . .	10
2.8.1 Equivalent circuit model . . . . .	14
2.8.2 Radial section drawing dimensions . . . . .	15
2.8.3 Clarke transform . . . . .	16
2.8.4 Three phase currents before Clarke transform . . . . .	17
2.8.5 Outputs currents of Clarke transform . . . . .	18
2.8.6 Rotating reference frame . . . . .	18
2.8.7 Direct and in-quadrature axis currents . . . . .	19
2.8.8 d-axis circuit model . . . . .	19
2.8.9 q-axis circuit model . . . . .	20
3.2.1 SMPM sections . . . . .	28
3.3.1 Simulation results . . . . .	30
3.3.2 Simulation results with a higher number of turns . . . . .	32
3.3.3 Torque comparison with and without skewing . . . . .	33
3.4.1 Convergence analysis . . . . .	34
3.4.2 Motor mesh slice . . . . .	36
4.1.1 Lamination material comparison . . . . .	39
4.2.1 Power losses in rotor region with laminated and solid solution . . . . .	40
5.1.1 Base frame format of a CAN string . . . . .	42
5.1.2 Voltage AND logic of the CAN bus . . . . .	42
5.1.3 Arduino acquisition system . . . . .	43
5.1.4 Fiat Panda 2nd series . . . . .	45
5.2.1 Altitude recorded by GPS . . . . .	46
5.2.2 Driving cycle GPS path . . . . .	47
5.2.3 Driving cycle power and slope path . . . . .	48
5.2.4 Fundamentals motor telemetry data . . . . .	49

5.2.5 Internal motor data . . . . .	49
5.3.1 Vehicle telemetry data . . . . .	51
5.3.2 Shaft speed VS GPS telemetry speed . . . . .	52
5.3.3 Battery pack monitoring data . . . . .	53
5.4.1 Shaft power calculated by MotorCad . . . . .	54
5.4.2 Efficiency map with drive cycle . . . . .	56
5.4.3 Total losses comparison with electrical steels M330-35A and M350-50A . .	56
5.5.1 Rotor stress FEM analysis . . . . .	58
5.5.2 Rotor total displacement FEM analysis . . . . .	59
6.2.1 Motor water jacket drawing dimensions . . . . .	63
6.3.1 Radial frontal section temperature distribution . . . . .	64
6.3.2 FEM axial temperature distribution . . . . .	65
6.3.3 Inlet and outlet drive system temperatures . . . . .	66
6.4.1 Magnetic model . . . . .	67
6.4.2 Magnets FEA analysis on critical load . . . . .	68
6.4.3 Demagnetization curve of magnets N30UH . . . . .	70
6.5.1 Axial section of the reviewed cooling jacket . . . . .	71
6.5.2 Temperature evolution in duty cycle thermal analysis with a redesigned cooling	72

# List of Tables

2.1	Hybridization factor classification . . . . .	9
3.1	Technical specifications . . . . .	24
3.2	Geometrical specifications . . . . .	24
3.3	Magnets specifications . . . . .	25
3.4	Overall motor sizes . . . . .	25
3.5	Stator geometry widths . . . . .	26
3.6	Stator axial lengths . . . . .	26
3.7	End winding dimensions . . . . .	27
3.8	Winding definition . . . . .	31
3.9	Mesh definition . . . . .	35
4.1	Technical specifications . . . . .	40
5.1	Drive CAN-Bus messages . . . . .	44
5.2	EPM CAN-Bus messages . . . . .	44
5.3	Vehicle characteristics . . . . .	45
5.4	Battery cells characteristics . . . . .	45
5.5	Duty cycle analysis . . . . .	55
5.6	Mechanical properties of materials used in the model . . . . .	58
6.1	Water jacket dimensions . . . . .	62
6.2	Fluid characteristic properties . . . . .	63
6.3	Critical working point . . . . .	68
6.4	Magnetic results at critical working point . . . . .	69
6.5	Magnetic results at critical working point . . . . .	69

# Chapter 1

## Introduction

Earth's changing climate has several impacts on the individual mobility, logistics and agriculture. In the last years many companies have been announcing their conversion to produce only zero-emission vehicles, this strong shift has been made possible thanks to the consumer sentiment, buffered also by the extended financial incentives, the growth in charging infrastructures and the expansion on the affordable models available. With the recent progress in the power electronics control, AC motors are suppressing almost all the applications in which the electric motors are involved. Research in magnetic materials has led to use of rare-earth magnets that enhances the motor power, but at the same time they are more prone to demagnetize under thermal stress. In the context of the Industry 4.0[1], which has been representing the fourth industrial revolution, refers to the continuous communication between machines and network in a way that prevents faults, programming maintenance and allows real time remote control. To integrate all components constitute this chain it is essential develop a platform in which all the information are collected, so the role of *big data* management and the *IoT* become crucial. Furthermore once these data are stored, in order to be able in problem solving or predict with precision the maintenance the *simulation* covers a central role.

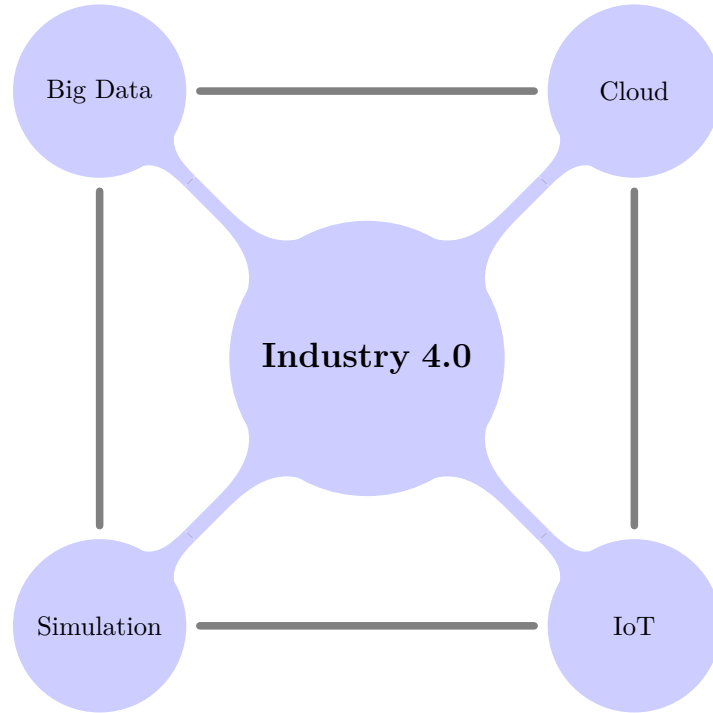


Figure 1.0.1: Industry 4.0 contents

This thesis aims to the remote monitoring of a full electric vehicle focusing on the motor and its component, looking for critical conditions, analyzing possible faults or evaluating severity of the found conditions. Thus, understanding the magnets properties demagnetization starting from the motor design and the data acquisition is evaluated. With the mechanical characteristics declared by the manufacturer, a permanent magnet synchronous motor (shortened PMSM) was designed following a reverse engineering procedure. Furthermore, data acquired by the Arduino based electronic platform are filtered and collected, separating the ones concerning the motor working and the vehicle ones. Through a post processing graphs analysis and linking data to the GPS path the correct operation of the motor is examined. If particular functioning conditions are observed, data acquired represent the input for the cycle simulation with the previously designed motor. The investigation aims to control thermal and magnetic behavior avoiding demagnetization faults, which determines costs related to magnets substitution and to machine down-time. Finally, the calculation of a simple performance index is proposed, with the aim of describing how far magnets are from their critical condition and if the heat is properly managed. This work allows a design review to make the motor suitable for the load condition required by the field. In this work is explored in Chapter 2 an overall description about electric motors types, focusing on the pro and cons of permanent magnet synchronous, the control logic and electromagnetic finite element analysis basics theory. The Chapter 3 describes the reverse engineering motor design starting from manufacturer's technical data and main

characteristics are discussed. To understand the materials influence on the motor functioning, Chapter 4 reports an overview and comparison among the different types and seeks to find which ones accomplish efficiency and best performance, neglecting related costs. In the Chapter 5, referring to the aforementioned context of the Industry 4.0, an electronic Arduino based system is realized to vehicle's data acquisition is presented, with a critical discussion on the analyzed data. Finally thermal design is examined, in Chapter 6 coupled thermo-magnetic FEM simulation has been done proposing also a thermal design review to optimize the heat exchange feature of the housing water jacket.



## Chapter 2

# Model of PM synchronous motor

### 2.1 Brief history of electric machines

The first experimental motors were described from a Scottish monk Andrew Gordon and American experimenter Benjamin Franklin in the *XVIII* century, focusing on electrostatic devices. One of the main problems was the difficulty from the electric circuit to provide high voltages required, so their development ends there. Invention of the electrochemical cells by *Alessandro Volta* paved the way to research in more efficient accumulator, which allows the availability of electric current till remains energy in the cells. Hans Christian Oersted was the first to discover links between electricity and magnetism: if a certain amount of current flows in a wire, it produces a magnetic field. In a very short time such important discoveries were carried out, like Ampere's law of induction between current-carrying wires, invention from Barlow of its wheel that proves the presence of Lorentz force causes the wheel to rotate about its axis. During the following years[2], the principal focus was the development of a DC motor, avoiding any conversion of current from the batteries, as later was necessary to drive AC motors. The main advantages of the DC motors were their reversibility in the use as motor or as generator, the ease to adjust speed by regulating DC voltage applied or using a pulse-width modulation duty cycle, but to work they need brushes to commute current every half revolution, otherwise the rotor would stabilize in an equilibrium position after half turn arranging themselves at  $90^\circ$  with magnetic flux direction. Instead, to regulate speed on AC motor a power inverter or variable frequency drive is needed. Due to the contact, brushes are very often subjected to critical damage and so, it has been necessary the research for other solutions to eliminate sliding contacts. Thanks to the discovery of rotating magnetic field, produced by poly-phase currents out of phase by a precise angle. The speed of its rotation is determined by the frequency of the alternating current. On this principle the asynchronous induction motor by Nikola Tesla with shorted winding rotor is based and then the synchronous one with permanent magnets .

## 2.2 Types of motors

Starting from the current source motors can be split in two different categories

- DC motors
- AC motors

### 2.2.1 DC motors

The first type are the easiest to built, it is based on the interaction between permanent magnets on the stator and induced magnetic field of the rotor. The electromagnet is made by a coil wound on iron core which convey the flux: when the current pass through windings, according to Lorentz's law as is shown in 2.2.1, generates a force  $\vec{F} = q \cdot \vec{v} \otimes \vec{B}$ . Hence, after half cycle, the currents polarity needs to be changed and so, forces applied on the rotor change. Brushes accomplish the described function and are subjected to spoilage during the motor functioning and produce sparks which may be dangerous if the motor is used in particular applications .

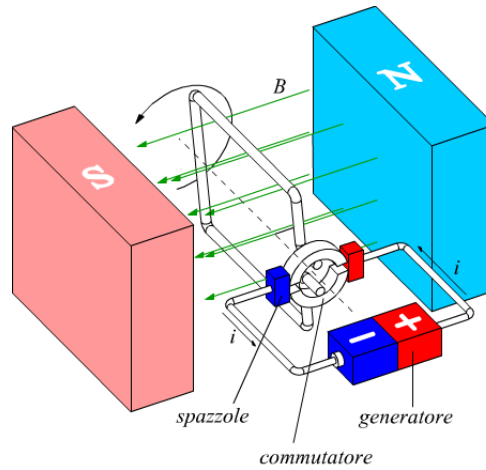


Figure 2.2.1: Working principle of a DC motor [3]

### 2.2.2 AC motors

To overcome problems related to brushes, the use of alternating current has taken hold. Two configuration of motor have been developed:

**AC induction motors** In the stator three-phase winding a rotating magnetic field is generated, in line with *Faraday-Neumann* induction's law

$$\Phi_B = \iint_{\Sigma(t)} B(t) \cdot dA \quad (2.2.1)$$

$$\mathcal{E} = -\frac{d\Phi_B}{dt} \quad (2.2.2)$$

where  $\mathcal{E}$  is the back electromotive force (henceforth called BEMF) produced in slip ring either in squirrel cage rotor, depending from the used type, is opposed to the magnetic field generated by the stator winding (according to *Lenz's law*). Since induced currents exist only with a time varying magnetic flux  $\phi_B$ , a relative velocity between the rotating magnetic field and rotor is necessary, this difference is called *slip*  $s = \frac{\omega_s - \omega_r}{\omega_s}$ . Since the working principle of asynchronous motor is inducing high value of currents to produce high power of motor too, the efficiency results limited due to the heat generated by windings on the rotor.

**AC synchronous motor** This type of motor are based on permanent magnets, embedded in the rotor or mounted on the rotor's surface. The magnetic flux generated by PMs<sup>1</sup> interacts with the one generated by stator windings, in this way the rotor follows the rotating field. The regulation is made by controlling both torque and velocity, by acting on the frequency of alternating currents loops from the inverter or with a flux-weakening control [4]. The main limitation of this type of motor lies in demagnetization of magnets, so the design of cooling system is particularly important, that will be addressed in later chapters. Permanent magnets can be mounted either on the surface of the rotor itself

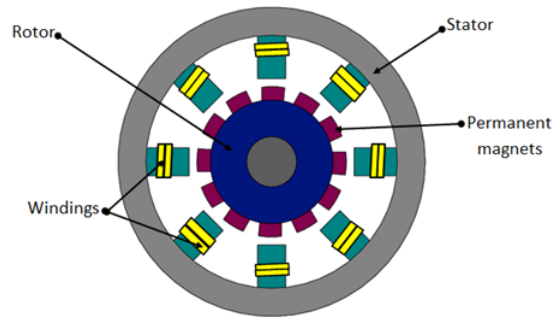


Figure 2.2.2: AC synchronous motor [5]

or embedded into it. The first are *surface mounted permanent magnets*, called shortened *SMPM*, the more affordable solution because production of rotor laminations not require further machining, as instead are required by the laminations used for *interior permanent magnet synchronous motors* (IPMSM). Besides, SMPM allows an easy magnets assembly just by sticking them in the caves, on the contrary dealing with IPMSM, magnets need to be inserted in the pockets of rotor laminations, with a consequently growing difficulty as the motor length increases. However, when costs are not a evident problem and high performance wants to be achieved, the production is on large scale (e.g. automotive manufacturers) and high speed revolution are requested, IPMSM are the best choice. Recently a rising interest on improvements of SMPM application field, allows the use also in high speed range, for example by adopting solutions which consists in magnet retaining sleeve [6] made as roll mill of steel or carbon fiber.

<sup>1</sup>Stands for Permanent Magnets

**SynRM** Alternatively to permanent magnets motors are the synchronous reluctance motors, based on *Hopkinson's* law

$$\mathcal{F} = \mathcal{R} \cdot \Phi_B \quad (2.2.3)$$

where  $\mathcal{R}$  measures tendency of a material to opposes against a magnetic field. The working principle of SynRM consists in an armature moving in a magnetic field which tends to align toward direction of minimum reluctance. The rotor laminations are designed with a path for the magnetic field made with high permeability and low power loss steel, in order to achieve great efficiency, flux barrier are made with air instead. Furthermore [7], several researches try to develop some hybrid solutions with SynRM motors are built using also magnets in the air pockets.

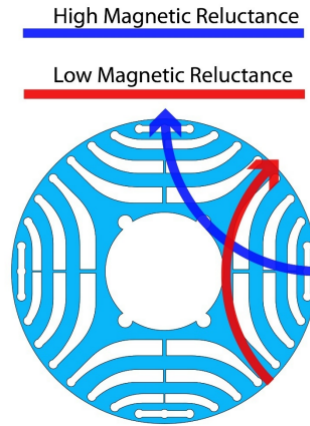


Figure 2.2.3: Synchronous reluctance motor [8]

## 2.3 Hybrid vehicles

Over the last decade, different approaches are tried to combine properly the electric power unit and internal combustion engine in order to achieve high performance and efficiency. The greatest vehicles manufacturers have tried to develop their own solutions, by classifying the mechanical connection of the motors on the shaft or with the power of the electric motor related to the internal combustion engine one. The first distinction analyzed, concerns the power of the electric motor compared with the nominal power of the internal combustion engine. The definition of the Hybridization factor [9] allows to understand of the most common technologies known:

$$HF = \frac{P_{EM}}{P_{EM} + P_{ICE}} \quad (2.3.1)$$

Use of different sizes of electric motors leads to the following classification:

Architecture	HF ratio
Micro hybrid	< 5%
Mild hybrid	5 ÷ 10%
Full hybrid	10 ÷ 75%
Full electric	100%

Table 2.1: Hybridization factor classification

By considering the shaft configuration can be made a further distinction:

**Parallel hybrid:** In this solution[10] the electric motor supports the ICE operation and are both connected to the drive shaft: when a boost is requested by the ICE, the electric motor turns on. The possibility to drive in pure electric mode is given by a clutch which decouples the EM from the ICE. Furthermore, the electric motor itself can commute as generator allowing regenerative braking.

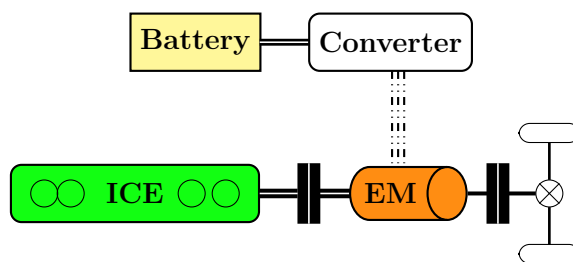


Figure 2.3.1: Parallel hybrid logic

**Series hybrid:** In this configuration. Only the electric power unit is connected to the shaft, instead the internal combustion engine turns the generator which charges batteries propelling so the EM. Nowadays this type is commercially found as Plug-in hybrid, to highlight the recharge from external power grid. Moreover, thanks to the ICE, the autonomy range is widely extended getting freedom from the batteries capacity.

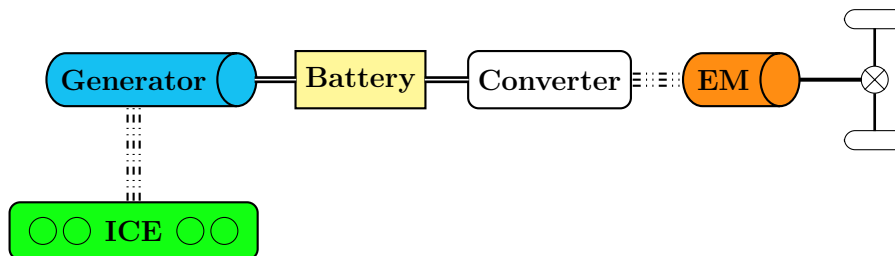


Figure 2.3.2: Series hybrid logic

In every application, the power of the motor needs to be proportionate to batteries capacity, considering the peak torque required to avoid excessive stress to battery cells[11]. Further research is focusing on new battery typologies .

## 2.4 Full electric vehicles

Recently, several attempts to replace the internal combustion engine are carried out, using hydrogen fuel-cells, solar panels to produce electricity or using battery to store it from an external source. In this section, the attention goes to electric vehicles mounting battery pack and uses permanent magnets synchronous motor to convert electric energy into mechanical one. Also known as BEV (battery electric vehicle), they have made their own way thanks to strong progress of the power electronics[12]. The prototype of electric vehicle accounted in this thesis is composed as follow:

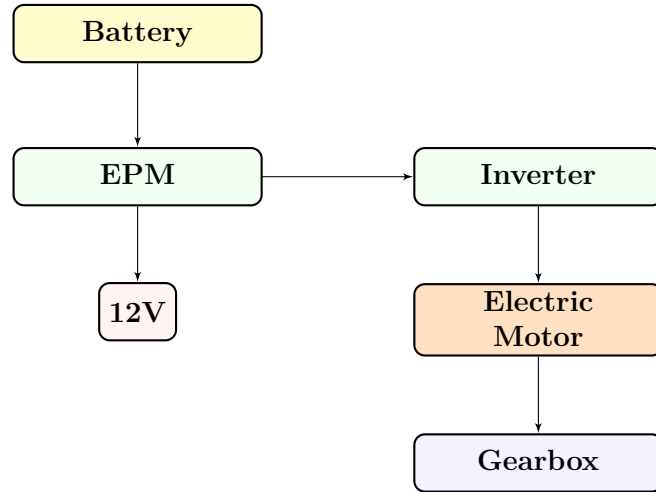


Figure 2.4.1: Logic box of a BEV

- EPM: stands for "Electronic Power Module", basically is a DC-DC converter which has double function of safety feature and voltage regulator, i.e. case in which power electronics fails to drive the motor. In addition, it decouples battery from the drive line and delivers different output voltages: 12V DC vehicle for onboard instruments and the one requested by the inverter. [13]
- Inverter: it's task is the conversion DC current in AC three-phase, which is delivered to stator winding terminals. It is mainly composed of transistors IGBT<sup>2</sup>, with their

---

<sup>2</sup>Transistors can be of three types: BJT (bipolar junction) is a current controlled device, FET (field effect transistor) is on the contrary a voltage controlled device, whereas IGBT (insulated gate bipolar transistor) can be driven by both of them and is designed to high power delivery.

fast switching speed are capable to obtain the target frequency to drive the rotation of magnetic field and so the motor itself.

Moreover, inverter module box has the dual function: is used to delivery power coming from the batteries (DC-AC) to the motor and to charge them with power delivered from the charging station, by converting it from AC current into DC one. To regulate speed a reference set point is sent from the driver through accelerator pedal, this number is converted in voltage (configured within 0-10V range) read by control unit. The set point is reached changing the three-phase current frequency, while the currents magnitude depends on the load, because it is directly connected with  $K_t$ <sup>3</sup> value of the motor. A feedback control on rotor position is implemented in order to deliver properly the currents to each phase and so to obtain the *phase angle* between  $I_d$  and  $I_q$ <sup>4</sup> equal to 90°. Rotor position is so controlled from an Encoder or a Resolver<sup>5</sup> mounted on the rotor's shaft.

## 2.5 Working principles

As previously explained a permanent magnet synchronous motor bases its working principle on the interaction between constant magnetic field of the permanent magnets and the rotating one produced by stator windings. Considering the expression of power as  $P = C \cdot \omega$  there are two ways to produce it: increase torque or increase revolution's speed. Every time a design occurs, it is necessary to find a trade-off among motor's size and costs of electronics will drive it. Torque scaling with dimensions as

$$T = kD^2L \quad (2.5.1)$$

since in this work it has been considered a radial flux motor,  $D$  is the rotor diameter and  $L$  is the axial rotor length. In a permanent magnet motor there are two contributes for the torque production, a first made by the natural behavior of the magnetic flux to align following the minimum resistance path, called as *Reluctance torque*, the second one is the *Cogging torque*, an undesirable contribute due to the self-alignment of the magnets with respect of the stator teeth. Thus, many strategies are deployed to reduce these undesirable contributes. On the other side, there is the contribute on which is mainly based the torque production in PMSM: coil wrapped on magnetic core of the stator, behave as electromagnets when they are crossed by currents creating north and south poles. It is straightforward that opposite poles are attracted to each other, on this force times the rotor radius is based the torque. This part is called *Alignment torque* or *Mutual torque*. When a motor is designed, it is worthwhile to take into account the basic difference on the angles defined. Talking about revolution, it is common referencing to *mechanical degrees*

---

<sup>3</sup>It is the proportionality coefficient between torque and current  $T = K_t \cdot I$

<sup>4</sup>They are the two components of the armature current in the rotating reference frame, as shown in Fig.2.8.6

<sup>5</sup>Both of them have the same function, they control speed and angular position of the rotor, but while Resolver is based on induction's principle and has analog signal, Encoder instead is optical and its accuracy depends on the disk provided and its signal has a square wave shape. For motor's application is preferred Encoder thanks to its high accuracy than Resolver.

$\theta_m$ , whereas, given the rotor in the same magnetic field direction is refer to *electrical degrees*  $\theta_e$ . Torque is proportional to the number of magnets placed on the rotor, so appear easy to increase this parameter, but if the use is provided for high speed also the frequency needs to follow the rotor. First is explained the correlation between angles:

$$\theta_e = \frac{N_m}{2}\theta_m \quad (2.5.2)$$

if are made derivatives with respect to time the relation is extended to velocities and again dividing by  $2\pi$  is found the frequency relation. Knowing also that

$$\omega_m = \frac{2\pi}{60}n \quad (2.5.3)$$

$$f_e = \frac{N_m}{120}n \quad (2.5.4)$$

so this means that the more is  $N_m$ , the more is the switching frequency and so the power electronics cost. As later is described about the motor concerned, since it is operating range at high speed, a lower number of magnet will be taken into account.

## 2.6 Magnetic theory reminders

Dealing with magnetic field, it is necessary to spend some words about the principal laws that govern it. A system composed by four partial differential equations was formulated first by Maxwell in 1865, reported below as integral and local expressions, among these, two are related to flux (surface integral), two related to closed loop (line integral) instead:

1. 
$$\oint_{\delta V} \vec{E}d\vec{S} = \int_V \frac{\rho}{\epsilon_0}dV \rightarrow \nabla \cdot \vec{E} = \frac{\rho}{\epsilon_0} \quad (2.6.1)$$

2. 
$$\oint_{\delta V} \vec{B}d\vec{S} = 0 \rightarrow \nabla \cdot \vec{B} = 0 \quad (2.6.2)$$

3. 
$$\oint_{\Gamma} \vec{E}d\vec{l} = -\frac{d\vec{\Phi}_B}{dt} \rightarrow \nabla \times \vec{E} = -\frac{\delta\vec{B}}{\delta t} \quad (2.6.3)$$

4. 
$$\oint_{\Gamma} \vec{B}d\vec{l} = \mu_0 \left( i_c + \epsilon_0 \frac{d\vec{\Phi}_E}{dt} \right) \rightarrow \nabla \times \vec{B} = \mu_0 \vec{J} + \mu_0 \epsilon_0 \frac{\delta\vec{E}}{\delta t} \quad (2.6.4)$$

In electric motors, following 2.6.4 alternating currents flowing in stator windings results in a consequent magnetic flux density  $\vec{B}$ , thus, considering the following relations:

$$\vec{B} = \mu \vec{H} \quad (2.6.5)$$

where  $\mu$  represents the product of  $\mu_0 \cdot \mu_r$ , so the magnitude of  $\vec{B}$  depends on material properties.

Force and so torque production is based on *Lorentz's* law which states:

$$F = q\vec{v} \times \vec{B} \quad (2.6.6)$$

given  $v = \frac{dl}{dt}$  and  $i = \frac{dq}{dt}$  and passing to infinitesimal values:

$$d\vec{F} = i\vec{B}dl \quad (2.6.7)$$

the total force exerted by a conductor of a length  $l$  is:

$$F = \int_0^L iBdl = BLi \quad (2.6.8)$$

## 2.7 Computational electromagnetics

When it concerns electric motors, or more in general electric machines (like transformers), are needed thorough results obtainable by discretizing the operating system. It seems obvious that a discrete parameters approach may be shallow and shows a different situation from reality conducting to bad evaluations. In this context FE method helps to bypass the resolution of partial differential equations, by using a mathematical functional, solving at the end algebraic equations in very small domain. First step is the introduction of finite elements method in Maxwell's equations[14] by defining the vector potential  $\vec{A}$ . Considering that  $\nabla \cdot \vec{B} = 0$  and taking into account that the divergence of a curl is zero, there must be a field such that:

$$\vec{B} = \nabla \times \vec{A} \quad (2.7.1)$$

substituting into 2.6.3:

$$-\nabla \times \left( \vec{E} + \frac{\delta \vec{A}}{\delta t} \right) = 0 \quad (2.7.2)$$

concerning the electric field, with the same logic as the definition of vector potential, is defined the scalar potential as:

$$\vec{E} = -\nabla V - \frac{\delta \vec{A}}{\delta t} \quad (2.7.3)$$

Introducing these relations in the Maxwell's equations, the system depends just by  $V$  and  $\vec{A}$ . Calculating these quantities from:

$$\vec{A} = \int \frac{\mu \vec{J} dv}{4\pi R} \quad (2.7.4)$$

$$V = \int \frac{\rho_v dv}{4\pi \epsilon R} \quad (2.7.5)$$

In order to solve the equations, physical system must be discretized in finite volumes, task called *mesh*.

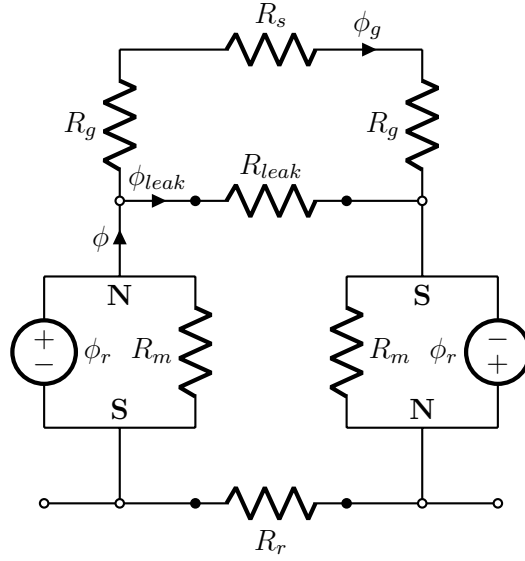


Figure 2.8.1: Equivalent circuit model

## 2.8 Electrical model

In the above picture 2.8.1 is shown the equivalent magnetic model circuit of a PMS motor, the resistances shown are *Reluctance* and measures the permeability of material to withstand a magnetic flux:

$$\mathcal{R} = \frac{l}{\mu A} \quad (2.8.1)$$

are represented:

- $R_r$  relative to the reluctance of the rotor steel
- $R_g$  related to the reluctance of the stator lamination
- $R_m$  and  $\phi_r$  are related respectively to the flux generated by the permanent magnets and their reluctance
- $\phi$  is the total flux available,  $\phi_g$  is the one flowing through the air gap,  $\phi_{leak}$  is a leak from one magnet to the other

from this model a further evaluation is done on the space needed to use all the available flux avoiding the material saturation. By stating the amplitude of the air gap flux density  $B_g$ , radius both of the rotor and the stator, the lamination length, main geometry parameters necessary to carry the flux within the motor are obtained.

$$\phi_{tot} = B_g A_g \quad (2.8.2)$$

where  $A_g = 2\pi R_{rot} L_{lam}$

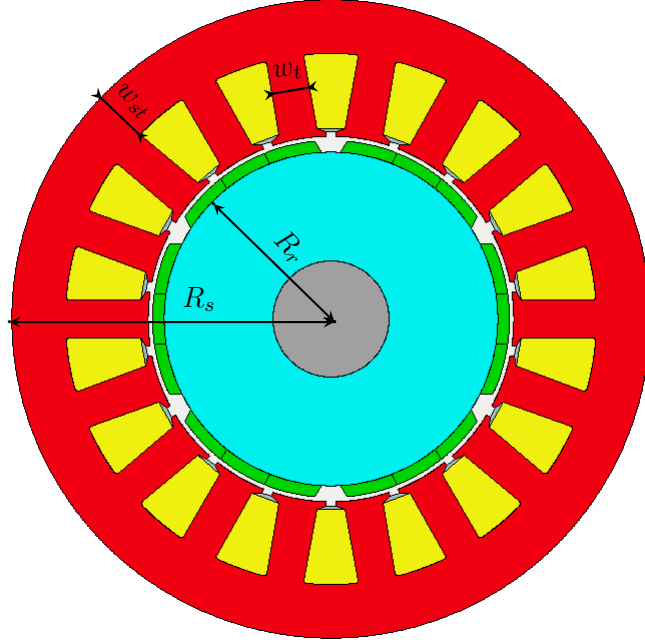


Figure 2.8.2: Radial section drawing dimensions

this flux is the total found in the air gap and is conveyed in rotor teeth. Since a motor have  $N_s$  stator slots, the magnetic flux in each tooth is

$$\phi_t = \frac{\phi_{tot}}{N_s} \quad (2.8.3)$$

considering that flux is the magnetic flux density  $B$  times the area normal to the flux direction  $A_{th} = w_{tooth}L_{st}$ , so the tooth width is:

$$w_{tooth} = \frac{\phi_t}{A_{th}} \quad (2.8.4)$$

Concerning the stator back iron width<sup>6</sup>, a further consideration can be done: every flux coming from each magnet  $\phi_m$  is divided in two halves and is closed in the south pole of the closest magnet. The width of the back iron is important, otherwise there is a poor interaction between poles, a lack of sufficient space could saturate the iron, leading to avoidable losses. In this way the stator back iron width is calculated, considering the magnitude of magnetic flux density  $B_s$  which depends on material used:

$$w_{rstat} = \frac{\phi_m}{L_{lam}B_s} \quad (2.8.5)$$

Rotor in the PMS motor could be made in two different configurations:

---

<sup>6</sup>It the region behind the slots, used to convoy fluxes

- Laminated
- Solid

As later is well explained, the main differences are on the losses. Usually, a laminated rotor is chosen when the axial length is quiet limited, where the dynamic behavior of the rotor don't raise instability phenomena. Increasing the axial length, the necessity of a more stiffness on the rotor becomes ever more important, thus a solid rotor solution is adopted. A further improvement to avoid an excessive heat generation due to the eddy current is to realize a spider shaft with arms carry the rotor steel core, allowing also a certain air flow inside the rotor itself and increasing convection. When a such type of rotor is used, also a radial width needs to be assessed. Identically as in the stator back iron width, taking into account the magnetic flux density saturation magnitude  $B_r$ :

$$w_{rot} = \frac{\phi_m}{L_{rot} B_r} \quad (2.8.6)$$

With this preliminary sizing, a first software based design can validates lengths calculated or allows to adjust it if there are inadequate.

### 2.8.1 Direct and quadrature axis

Dealing with AC synchronous motors, power electronics transforms DC currents coming from batteries in three phase alternating ones. Power produced by alternating currents is made of two components called *active* and *reactive*:

$$P = V \cdot I \cos \phi \quad (2.8.7)$$

$$Q = V \cdot I \sin \phi \quad (2.8.8)$$

Active power is the one really consumed and used to produce work, instead, reactive power is continuously absorbed from the load and refunded to the energy source, it is useless and reduces the effective power of the motor. Control circuit needs to monitor the power factor  $\cos \phi$  to a value above 90%.

$$\mathcal{T} = \frac{V \cdot I \cos \phi}{\omega} = \frac{const \cdot \Phi \cdot I \cos \phi}{\omega} \quad (2.8.9)$$

So the control operating logic works transforming first the three phase currents in two phase currents with the *Clarke* transform:

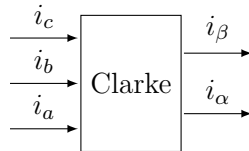


Figure 2.8.3: Clarke transform

$$\begin{cases} i_a = I \sin(\omega t) \\ i_b = I \sin(\omega t + 2\pi/3) \\ i_c = I \sin(\omega t - 2\pi/3) \end{cases} \quad (2.8.10)$$

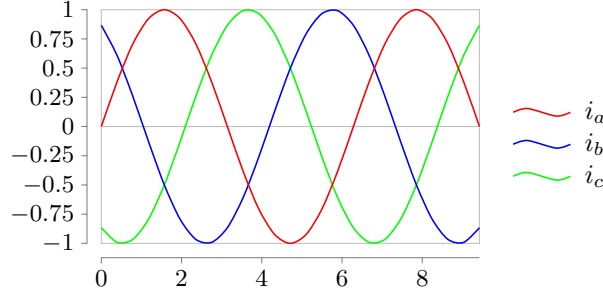


Figure 2.8.4: Three phase currents before Clarke transform

Furthermore, by adding a zero axis, such as the sum of a three phase balanced currents is equal to zero:

$$i_0 = k_1 k_2 (i_a + i_b + i_c) \quad (2.8.11)$$

so the transform operates as a matrix product:

$$\begin{bmatrix} i_\alpha \\ i_\beta \\ i_0 \end{bmatrix} = k_1 \begin{bmatrix} 1 & -\frac{1}{2} & \frac{1}{2} \\ 0 & \frac{\sqrt{3}}{2} & -\frac{\sqrt{3}}{2} \\ k_1 & k_2 & k_3 \end{bmatrix} \begin{bmatrix} i_a \\ i_b \\ i_c \end{bmatrix} \quad (2.8.12)$$

substituting 2.8.10 into 2.8.12 and finding  $k_1, k_2, k_3$  constants:

$$\begin{bmatrix} i_\alpha \\ i_\beta \\ i_0 \end{bmatrix} = \sqrt{\frac{2}{3}} \begin{bmatrix} 1 & -\frac{1}{2} & \frac{1}{2} \\ 0 & \frac{\sqrt{3}}{2} & -\frac{\sqrt{3}}{2} \\ \frac{1}{\sqrt{2}} & \frac{1}{\sqrt{2}} & \frac{1}{\sqrt{2}} \end{bmatrix} \begin{bmatrix} I \sin(\omega t) \\ I \sin(\omega t + 2\pi/3) \\ I \sin(\omega t - 2\pi/3) \end{bmatrix} \quad (2.8.13)$$

furthermore, defining  $i_\alpha = i_a$ , by make matrix products, is finally found formula:

$$\begin{cases} i_\alpha = i_a = I \sin(\omega t) \\ i_\beta = I \sin(\omega t + \pi/2) \end{cases} \quad (2.8.14)$$

Ones Clarke transform is applied, another step to control properly currents is required. Reading angle position  $\theta$  from the resolver, the reference frame is changed and is anchored to the rotor position, so it rotates at same speed. This is made with Park transform, with definition of  $i_d$  and  $i_q$  currents: these two quantities represents the projection on  $d$  and  $q$  axis of the armature current. Direct axis is on direction of minimum reluctance, while in quadrature axis is perpendicular to the first.

From the figure 2.8.6 the links between  $\alpha, \beta$  frame and  $d, q$  frame are straightforward:

$$\begin{cases} i_d = i_\alpha \cos(\theta) + i_\beta \sin(\theta) \\ i_q = -i_\alpha \sin(\theta) + i_\beta \cos(\theta) \end{cases} \quad (2.8.15)$$

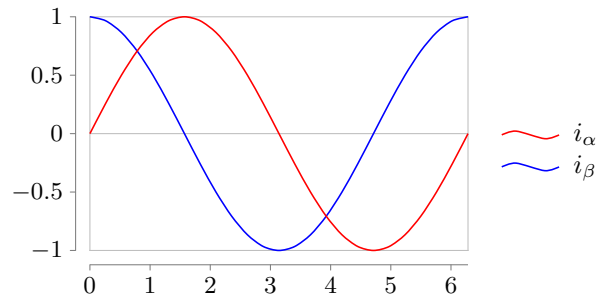


Figure 2.8.5: Outputs currents of Clarke transform

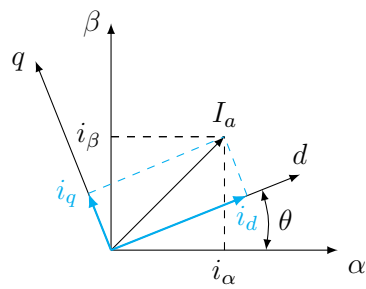


Figure 2.8.6: Rotating reference frame

For the sake of clarity, the resulting currents are graphically shown in the figure below .

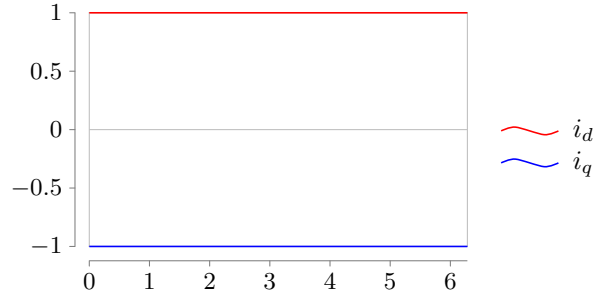


Figure 2.8.7: Direct and in-quadrature axis currents

### 2.8.2 Torque production

In order to determine the fundamental laws that govern the torque production in a permanent magnet synchronous motor, a sketch of an equivalent circuit needs to be analyzed.

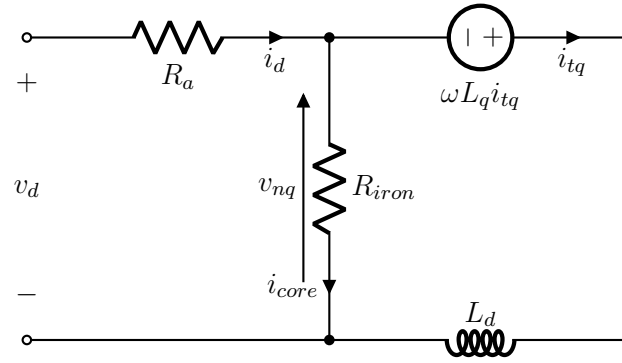


Figure 2.8.8: d-axis circuit model

In the above pictures, direct and in-quadrature stator currents are divided in iron current which conducts inevitably to losses and the one produces torque. These equivalent models conduct to equations obtained by applying Kirchhoff's law:

$$\begin{cases} v_d = R_a i_d - \omega L_q i_{tq} \\ v_q = R_a i_q + \omega L_d i_{td} \end{cases} \quad (2.8.16)$$

The flux in  $dq$  axis are expressed as:

$$\begin{cases} \Psi_d = L_d i_{td} + \Psi_f \\ \Psi_q = L_q i_{tq} \end{cases} \quad (2.8.17)$$

So the torque equation is found:

$$T = p(\Psi_d i_{tq} - \Psi_q i_{td}) = p[\Psi_f i_{tq} + (L_d - L_q) i_{td} i_{tq}] \quad (2.8.18)$$

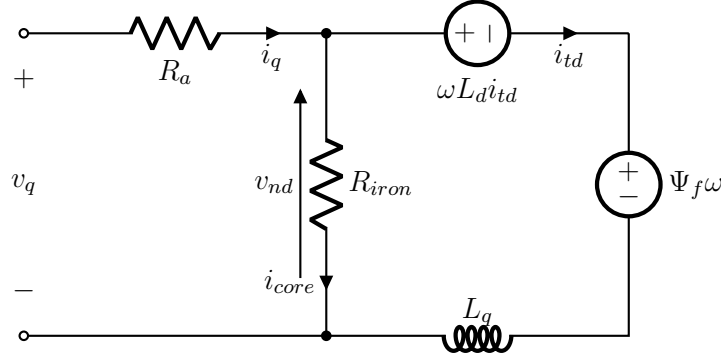


Figure 2.8.9: q-axis circuit model

Where  $\Psi_f$  is the magnetic flux of a single magnet,  $L_d$  and  $L_q$  are the d-axis inductance and q-axis inductance,  $\omega$  is the angular velocity of the rotating magnetic field,  $p$  is the number of magnetic poles. In a surface mounted permanent magnets motor, there are no substantial differences between the inductance in quadrature axis, so the assumption  $L_d = L_q$  is reasonable. This means regarding torque:

$$T = p\Psi_f i_{tq} \quad (2.8.19)$$

The result evidences that is the only q-axis current leads to torque, while the d-axis current is accountable of useless losses. Obviously the line current is  $i_l = \sqrt{i_d^2 + i_q^2}$ , this relation could be used to find fails in the power electronics unit. If in a moment for some reason, phase between  $i_d$  and  $i_q$  is not anymore  $90^\circ$ , so  $i_q$  will drops, since the motor is set either in speed or torque reference, in order to withstand the load the drive will absorb more and more current until it reaches the set point.

## 2.9 Motor constant

To underline the main parameters involved during the operation of electric motors, three main constants are defined.

### 2.9.1 Back EMF constant

As Faraday's law states, a time variation of magnetic flux produces an electro-magnetic force in the nearby conductors, if the airgap flux is expressed as:

$$\Phi_g = B_g \cdot A_g = B_g R_{rot} \theta_p L_{stat} \quad (2.9.1)$$

by substituting into Faraday's law:

$$B_{EMF} = \frac{d\lambda}{dt} = \frac{d\theta_e}{dt} \cdot \frac{d\lambda}{d\theta_e} = \frac{N_m}{2} \omega_m \frac{2N\Phi_g}{\pi} \quad (2.9.2)$$

is so achieved:

$$B_{EMF} = 2NB_g L_{stat} R_{rot} \omega_m = K_e \cdot \omega_m \quad (2.9.3)$$

Thus, the contributions to  $BEMF$  can be split in three main parameters:

$2N$  stands for the number of conductors and two slots facing have  $N$  conductors

$B_g$  is the airgap magnetic flux density, depending both on number of turns per coil and by the type of magnets placed on the rotor

$L_{stat}R_{rot}$  are the main geometric parameters

$\omega_m$  highlights a strong influence by rotor speed

$K_e$  is usually referred to the peak line voltage, whose units are  $\frac{V}{rad_M/s}$ , even if many manufacturers prefer to use the RMS value of the line-line back EMF.

### 2.9.2 Torque constant

Considering the power balance as:

$$\omega_m \mathcal{T} = B_{EMF} \cdot i \quad (2.9.4)$$

and dividing by the angular velocity and substituting 2.9.3:

$$\mathcal{T} = 2NB_g L_{stat} R_{rot} = K_t \cdot i \quad (2.9.5)$$

In this case, since alternating currents are involved, the RMS value is so significant then the peak one, whose units is  $\frac{Nm}{A_{RMS}}$ .

### 2.9.3 Motor constant

The above constants are related to the waveform, losses, and are not able to compare two different electric machines. Motor constant measures the motor's ability to convert the electric power into a mechanical one. It can be defined as:

$$K_m = \frac{\mathcal{T}}{\sqrt{P}} \quad (2.9.6)$$

where  $P = Ri^2$ , so become:

$$K_m = \frac{K_t \cdot i}{\sqrt{Ri^2}} = \frac{K_t}{\sqrt{R}} \quad (2.9.7)$$



# Chapter 3

## Motor design

### 3.1 Electro-magnetic target specification

In a design of electric motors are requested as starting points some characteristics:

- Size
- Power
- Speed
- Voltage DC Bus

First geometry is assumed, since the torque vs size relation follows 2.5.1. Torque is more sensible to a diameter increase with respect to the motor length, but one of these can be constrained to the applying specifications. Moreover, also the application field decides both the power involved and the speed: e.g. in the full electric and series hybrid automotive driveline architectures, the speed range is so large for two reasons: first in order to have a larger regulation span, since usually the electric motor is provided with a fixed reduction gearbox that replaces the common transmission, in this way the driver can achieve a certain power with a precise regulation; the second one is strictly coupled with the torque produced within a specified size. Power is  $P = \mathcal{T} \cdot \omega$ , this means that if the maximum torque is already achieved, the only way to reach the target power is to increase speed. On the other side, in parallel hybrid vehicles, the electric motor is coupled with the internal combustion engine, so it has to comply with its speed. In this situation the only way to increase torque, and so the power, is to reach high values of currents at the nominal point, thereby since  $T = K_t \cdot I$  torque is not increased with  $K_t$  but with  $I$ . Further investigations are made in a dedicated chapter on the rise of current, because there is a constraint on the maximum value of the current can withstand the magnets to avoid demagnetization.

In this work, a reverse engineering process, to rebuild the electric motor, knowing the following data reported in 3.1 is followed, in the 3.2 geometric specifications are reported instead, both are provided by the manufacturer:

Data	Value	Unit
Poles number	6	[-]
$n_{nom}$	9000	[rpm]
$P_{nom}$	43	[kW]
$C_{nom}$	45	[Nm]
$K_e$	0.2	$[\frac{V_{RMS}}{rad/s}]$
$BEMF_{nom}$	180	$[V_{RMS}]$
$K_t$	0.3	$[\frac{Nm}{A_{RMS}}]$
$I_{nom}$	150	$[A_{RMS}]$
$\eta$	0.92	[-]

Table 3.1: Technical specifications

Data	Value	Unit
$\phi_{ext}$	248	mm
$\phi_{shaft}$	30	mm
$L_{mot}$	280	mm

Table 3.2: Geometrical specifications

## 3.2 Stator design

In the first instance, the radius ratio  $R_{rot}/R_{stat} = 0.56$  [15] that maximizes motor constants has been established. Considering an integral slot motor, in this way the harmonics produced from each winding are in phase with each other, the total number of slots is found considering one coil per pole per phase. Taking the number of magnets  $N_m = 6$  from 3.2 and since the motor is fed with a three phase alternating currents  $N_{slot} = 18$ , hence the number of coil per phase is  $N_{slot}/N_{phase} = 6$  equal to the number of magnets. In this preliminary design, it is necessary to follow a general proportional rule, to identify the basic geometrical features. The stator yoke represents another important parameter, since its value comes out by a trade off between torque and the cogging torque produced by the motor: increasing air gap length lead to a decrease both in torque and in cogging one, but an opposite behavior is shown if the air gap is reduced. This phenomenon could be justified considering the flux balance along the stator yoke:

$$B_{rot}A_{rot} = B_g A_g \rightarrow B_g = \frac{B_{rot}A_{rot}}{A_g} \quad (3.2.1)$$

i.e. a rise in  $A_g$  conduce to a drop in  $B_g$ .

A good compromise is obtained if the stator yoke is equal to the half of the number of slots per magnetic pole [15]:

$$g = \frac{N_s}{2 \cdot N_m} \quad (3.2.2)$$

The last size that determines the overall geometric description of the motor is the

magnet thickness. Magnets are commercially sold with a proper thickness and arc length both selectable. If the air gap width and the arc are fixed, an increase in magnetic thickness determines a rise in the flux linkage both on D and Q axis while the axis inductances are reduced. Instead reducing magnetic thickness has the opposite effect on both phenomena. Virtually first aspect influenced by the flux linkage is increasing in torque, on the other hand a increase too much of this value involves in a rise of asymmetry, which makes  $L_d \neq L_q$  and so, as it is stated in 2.8.18, could affect the torque production. The second aspect investigated is the change in inductance on D and Q axis:

$$L = \frac{\Phi}{i} \quad (3.2.3)$$

because with a fixed arc length, increase in thickness results in volumetric growth, so the magnetic energy available is higher and so the flux from magnets, coupling this with the one produced by the coils results in a lower flux in the air gap, on which is based the inductance calculation. To whom it concerns about the magnets arc lengths this cannot never be equal to  $180^\circ E$  otherwise the flux coming from a north pole of a magnet would close in the beside one, it neither could be too narrow because there would be difficult the linkage with the stator flux. Thus, considering a commercially available magnets length of 40mm, trade-off results are shown in the table below: With these specified size the overall

Data	Value	Unit
<i>Arc length</i>	150	<i>E deg</i>
<i>Thickness</i>	4	<i>mm</i>

Table 3.3: Magnets specifications

dimensions found are:

Data	Value	Unit
$\phi_{ext}$	220	<i>mm</i>
$\phi_{bore}$	126	<i>mm</i>
<i>Airgap</i>	1.5	<i>mm</i>
$\phi_{shaft}$	40	<i>mm</i>

Table 3.4: Overall motor sizes

Once a first geometrical draft is done, before simulations begin, the design of slots have a fundamental importance to:

- allow the entry of windings, so there will be a sufficient slot opening length, but not too much to make sure that the cogging torque remain low
- to avoid overheating, so the heat should be able to pass through the stator lamination reaching the cooling system
- give an adequate area to house conductors, but need to respect dimensions discussed in 2.8.

Hence, a Matlab script has been written to help the design process of this motor, the inputs used depend from materials considered, which are:

- Stator lamination M330-35A with  $B_{sat} = 2.1T$
- Air gap magnetic flux density  $B_g = 0.9T$

from which the following dimensions are found referring to 2.8.5 and 2.8.4:

Data	Value	Unit
$w_{rstat}$	18	mm
$w_{tooth}$	12	mm

Table 3.5: Stator geometry widths

For what is concerned the axial dimension of the motor, are known from the manufacturer datasheet the following specifications:

Data	Value	Unit
$L_{mot}$	280	mm
$L_{resolver}$	57	mm
$Mag_{rows}$	3	—

Table 3.6: Stator axial lengths

The design carried out has took into account the construction requirements for windings, i.e. when a coil winding is wound around a stator slot cage the turn needs a certain amount of space to curve and entry in the next slot, this space is called *end winding axial overhang* found both on the front and rear side of the motor. A sensitivity study also has been done on this parameter, so the results found are:

- increase the overhang winding lengths leads to rise up the winding resistance, and so the copper losses, conducting to a drop in efficiency, since these extremity parts do not produces useful work
- on the thermal side, reducing the coil head extension involves a decrease in heat sink function compromising the internal heat exchange

Knowing the axial length of a single magnet row  $L_{mag} = 40mm$  and considering their number from table 3.6, the active length of the motor is found:  $L_{mot} = 120mm$ , a good achievement is obtained with the following dimensions, leaving an available space for housing and structural supports.

The aforementioned hypothesis on the axial length of the motor conduces to the simulations reported. If is considered an uncertainty on the length of  $\pm 20\%$  and since the torque scales linearly with the axial length, as is stated in 2.5.1, there will be an associated

Data	Value	Unit
$Ewdg_{front}$	40	<i>mm</i>
$Ewdg_{rear}$	55	<i>mm</i>

Table 3.7: End winding dimensions

fluctuation on the torque. Each row of magnets is shifted by an angle  $\alpha$  used to reduce the cogging torque, this angle [16] is determined from:

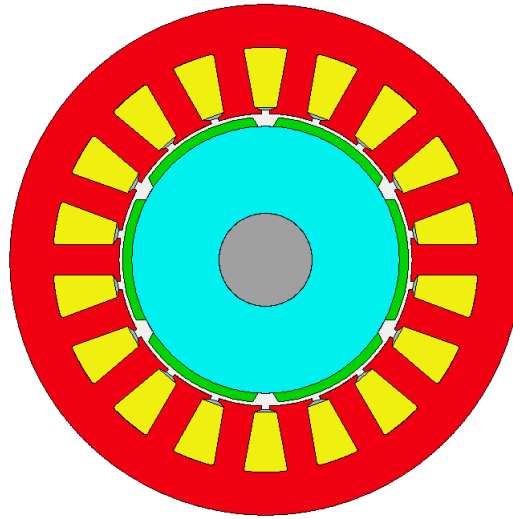
$$\alpha_{skew_E} = \frac{N_m}{N_s} \cdot 180 = 60 \quad [E \text{ deg}] \quad (3.2.4)$$

$$\alpha_{skew_M} = \alpha_{skew_E} \cdot \frac{2}{N_m} = 20 \quad [M \text{ deg}] \quad (3.2.5)$$

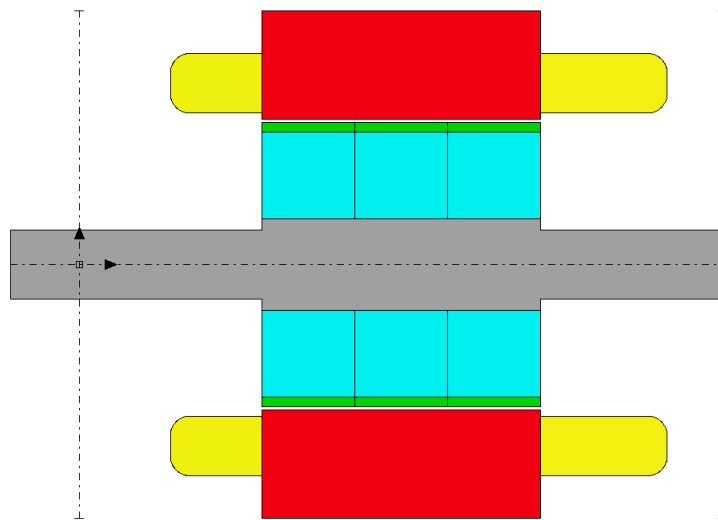
and each row is shifted of:

$$\alpha_{skew} = \frac{\alpha_{skew_M}}{N_{row}} = 6.67^\circ \quad (3.2.6)$$

with these geometry specifications is realized the motor model on Ansys MotorCad®: it is a multiphysics software, integrates Electro-Magnetic, Thermal, Lab and Mechanical modules allowing the design of different topologies of electric motors. The results are shown in the following pictures :



(a) Radial section of PMSM



(b) Axial section of PMSM

Figure 3.2.1: SMPM sections

### 3.3 Electromagnetic analysis of definitive motor configuration

#### 3.3.1 Brief discussion about attempts done before reaching the final configuration

Many attempts were done before reaching the final configuration, in which the electromagnetics and drive outputs data are comparable with the ones declared in datasheet by the

manufacturer. Maintaining as constants internal geometric data, other parameters could determine the performance of machine in term of power and voltage developed, such stator and rotor lamination material, otherwise magnets material that influences the magnitude of BEMF induced in stator winding coupled with number of turns, such as lamination thickness from which the material saturation and losses depends, so as the machine efficiency.

### 3.3.2 Guiding lines for motor design

Different configurations in number of turns and strands in hand are carried out, the focus is on the parameter  $\vec{J}$ , which stands for RMS current density, directly involves the phase resistance. The aim in the design process is to maintain this value below  $7 \frac{A_{RMS}}{mm^2}$ . Another way to control current density is to make parallel paths: each phase current is divided into a number of paths, in this way the current is also divided too and the current density is controlled. With this method a less number of wire in each turn is needed, so smaller slot area could be used, but a complexity in the production process is introduced and a number of critical point in which some issues may arise are introduced too. The easiest way to reduce  $J$  is build a bigger slot with respect to the previous one, in a way that increase the number of wire in each turn of winding. This solution surely reduces the number of turns feasible, but usually this not represents a relevant problem, since with a double layer winding the number of turns necessary to obtain the required back electromotive force is low. In order to make a comparative analysis, first are shown below the ultimate results in terms of BEMF and Torque. An important premise must be expressed, the remanence  $B_r$  of permanent magnets is function of temperature, so is needed to clarify the simulation conditions, in this way we are able to compare different configurations. Two ways are available: first using the convergence tool implemented in MotorCad to find the steady state condition in a coupled electromagnetic and thermal simulation, but the final temperature could be different by changing material, because every material has proper heat exchange coefficients, second by fixing an armature winding and magnet temperature. For example in a normal operating condition a motor should be at  $80^\circ C$ , so with these test conditions the following results are found:

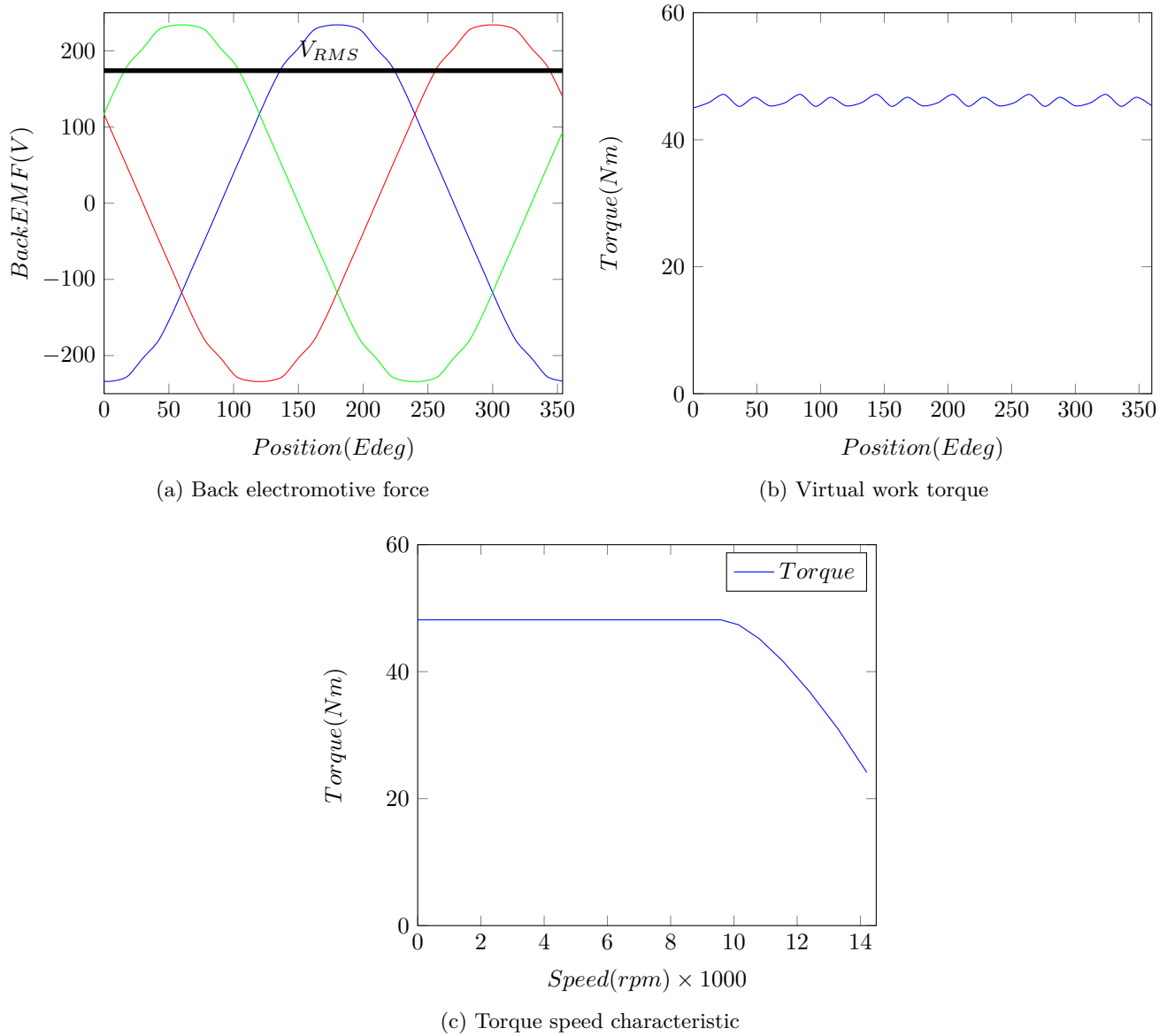


Figure 3.3.1: Simulation results

Looking at the charts, the results obtained concerning BEMF are in line with requests, the same is with the torque. The cogging torque is also reduced to 4% thanks to the magnets skewing. The efficiency obtained is  $\eta = 96.3\%$ . This model uses the following winding parameters:

Data	Value	Unit
$N_{turns}$	2	–
$Layers$	2	–
$N_{strands}$	70	–
$Cond/slot$	280	–
$\phi_{wire}$	0.885 – 0.800	$mm$

Table 3.8: Winding definition

In the previous attempts, other combinations of wire diameter, number of turns and number of strands are developed to find the optimum: with an higher number of turns there is just a grow in BEMF and so in torque, moving the knee of the  $C-\omega$  characteristic in fig 3.3.1c towards higher speeds, for example a previous attempt has been done with a double number of turns  $N_{turns} = 4$  and double layer winding, the result in terms of torque and BEMF are shown below:

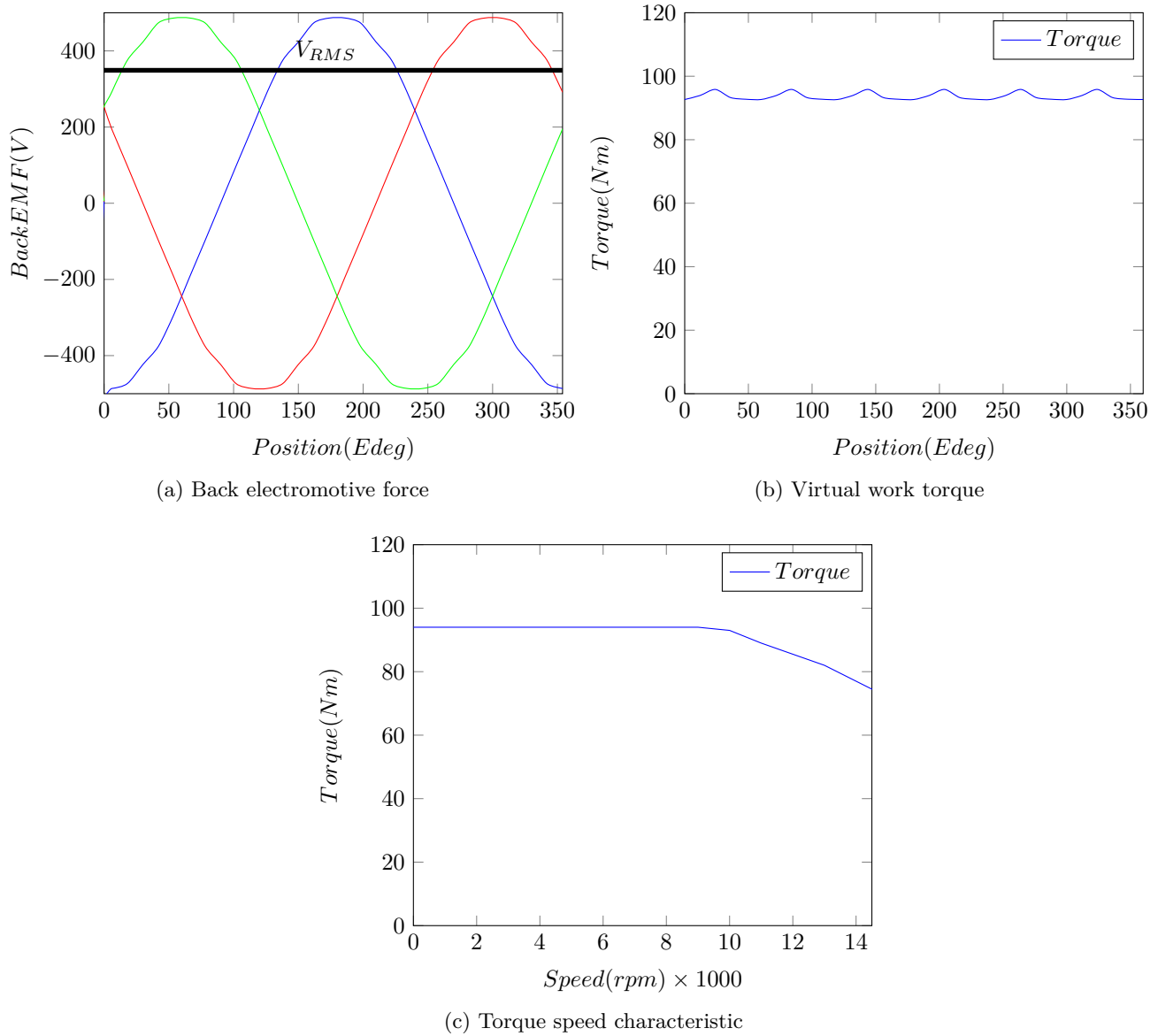


Figure 3.3.2: Simulation results with a higher number of turns

As it was expected, each value proportional to the number of turns rises up, as a consequence also the speed range at constant torque is extended. Thus, the requirement for such a motor is a higher value of DC bus voltage, if this is not achievable, there may show severe fault condition in the sense that the motor tends to act as generator, leading to irreparable damages [17] the inverter and the power electronics if fuse box is not well sized. The same considerations could be done on a lower number of turns and we will expect, with good approximation linearly, a reduction in torque, BEMF and a knee moved

to lower speed. Another worthwhile comparison is led on a motor with and without axial magnets skewing. Remembering what it was discussed in 3.2 i.e. cogging torque depends on the self alignment of the magnets and the stator teeth due to low reluctance as it is stated by Hopkinson's law 2.2.3.

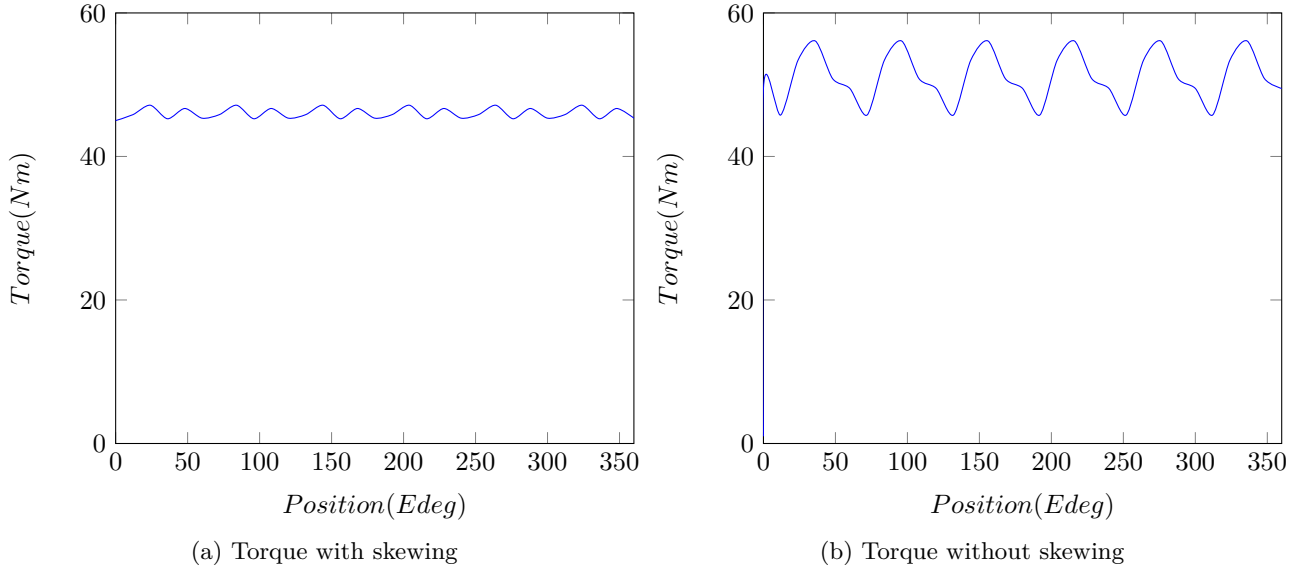


Figure 3.3.3: Torque comparison with and without skewing

The torque ripple is arranged on 4% in a skew magnets motor, compared to 20% in a not skewed one. Torque oscillations are accountable of undesirable vibrations with consequences on supports and power users which lifespan may be reduced. Furthermore, is to be taken into account that an internal combustion engine, within a four stroke just one develops power<sup>1</sup>, so a flywheel is mounted in order to stabilize speed fluctuations coming from the peak torque produced in the useful stroke. In parallel hybrid architectures since the electric motor is coupled with internal combustion engine, the torque ripple produced by this latter is greater, so the torque ripple of the electric motor coupled with may be not a relevant problem, instead in a full electric solutions either in industry field automation where is claimed precision in the positions achieved, ripples must be controlled and reduced properly. For the sake of clarity, skewing procedure influences also other quantities like BEMF, the result is on a less sinusoidal wave tending to a square one, more evident on a shorter motor since the reluctance effects are more significant.

<sup>1</sup>Four strokes of Intake-Compression-Power and Exhaust

### 3.4 Convergence analysis

Considering that the software uses a finite elements approach to analyze the model, is useful to understand the sensitivity to the mesh lengths in order to find a good compromise between a sufficiently precise results and calculation time. Several mesh lengths are adjusted to investigate their influence on results, there are:

- Stator lamination mesh length
- Stator slot mesh length
- Rotor lamination mesh length
- Magnet mesh length
- Minimum point mesh separation

Each length is intended as the length between mesh nodes in the region, the minimum point separation is a further measure controlled, means that if points are separated by a distance below this value, these are considered as a single point. Since the software offers the possibility to control the mesh in each region of the motor, may be useful to refine mesh in areas more critical subjected to sharp magnetic gradient as in the stator lamination, where also thermal simulation needs more accuracy due to the heat exchange with housing water jacket.

A sensitivity study analysis has been done in a way to highlights the effect of each mesh length to the output results, as it has been examined there are not many relevant differences in terms of electromagnetic power by use shorter mesh length, except for torque ripple, since it is composed by the sum of little forces acting in opposite directions. In the following graph is shown the trend of the electromagnetic power, because in this expression is contained the effect of integral calculations. It is noticed that, as it was expected,

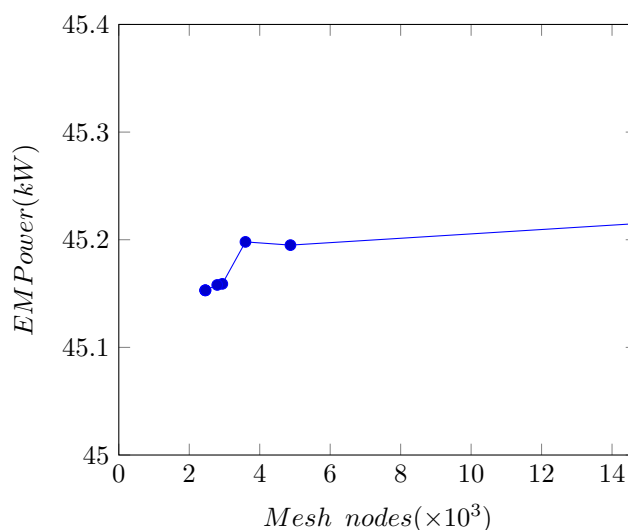


Figure 3.4.1: Convergence analysis

growing the number of nodes increases the accuracy until it reaches a steady value. Considering that a large number of nodes involves in high computation time with a little gain in precision, referencing to Fig.3.9 a trade off in the minimum of the curve must be found. In this point is ensured calculation accuracy and a controlled computation time. In order to obtain an adaptive mesh, the magnets need a finer mesh considering that they are subjected to rapidly changes in magnetic field produced by the stator windings, hence a different magnet mesh length is chosen. In the table below are reported the parameters used in calculation: In the following picture is shown a meshed motor slice, different mesh

Data	Value	Unit
<i>Stator lam</i>	1.5	<i>mm</i>
<i>Stator slot</i>	1.5	<i>mm</i>
<i>Rotor lam</i>	1.5	<i>mm</i>
<i>Magnet length</i>	1	<i>mm</i>
<i>Nodes num</i>	2889	–
<i>Element num</i>	5490	–

Table 3.9: Mesh definition

division allows the computation of more accurate results, and besides may show critical issues in terms of demagnetization.

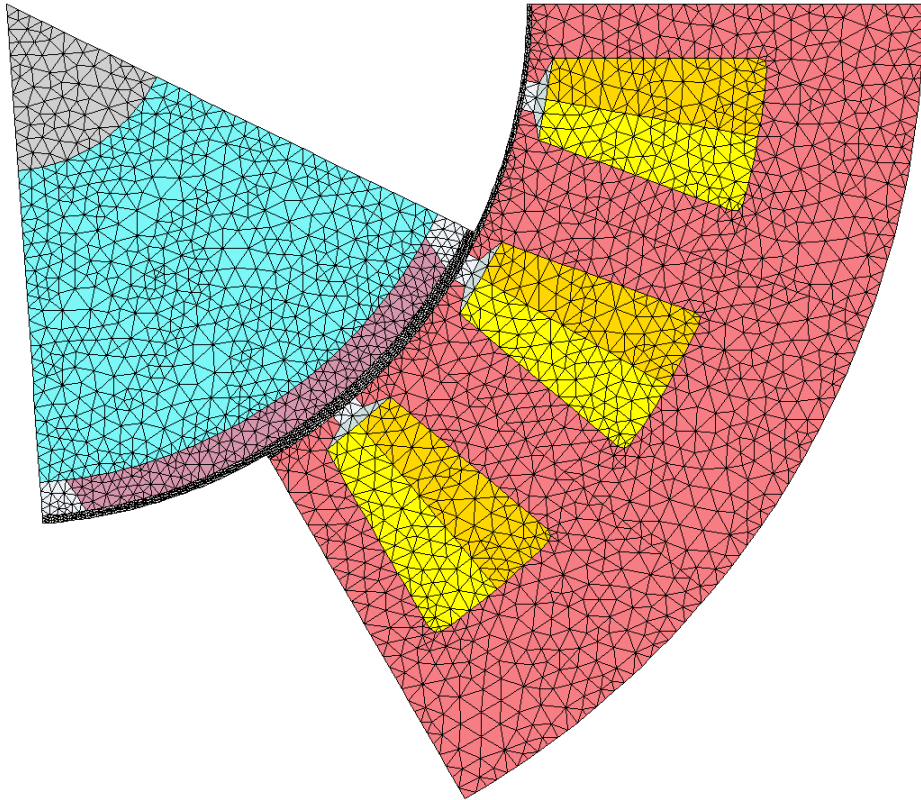


Figure 3.4.2: Motor mesh slice

## Chapter 4

# Comparative analysis of materials

As part of permanent magnet synchronous motors, different materials may be used to convey magnetic flux produced in windings and to keep low the power losses. Two main contributions increases losses: eddy currents and magnetic hysteresis. Eddy currents follows Maxwell's equation 2.6.3 so they are produced by a time varying magnetic field, instead, hysteresis losses occurs when a material is subjected to a cyclic magnetization: applying and reducing external magnetic field involves in thermal losses and this is due to the work spent on the re-orientation of magnetic domain after a magnetization. To evaluate magnitude of material power losses, several empirical models have been developed, in this discussion power losses are calculated by using *Steinmetz* model. This is a power equation which highlights the dependence of losses mainly on the frequency and contains coefficients which take into account the contributions both highlighted before:

$$P_w = k \cdot f^a \cdot B^b \quad (4.0.1)$$

where  $k, a, b$  are the Steinmetz coefficients depending on interpolation of material  $B$ - $H$  curve. The calculated  $P_w$  consists in a power on unit of mass  $\frac{W}{kg}$ . Usually, the kind of material used is called electrical steel, which is a ferromagnetic material made up with iron and silicon, its presence allows the increase in resistivity of the steel i.e. since  $P_w \propto Ri^2$  and  $i = \frac{V}{R}$  increasing resistance involves in a reduction of current  $i$  and so reduces iron losses. Silicon is added in a range of 1% ÷ 6.5%, a low value of silicon leads to high losses, instead a value too high of silicon makes the material brittle and unsuitable for cold rolling. Two different types of electrical steel are available:

- Grain oriented
- Non oriented grain

Dealing with electric motors, in which the direction of magnetic field is not fixed, but it varies as a function of time, presence of grain oriented steel [18] in the rolling direction of lamination could affects negatively motor performance, the advantages of this type of steel are high permeability with a very low energy losses, so are widely used in static

application such as transformers. Instead, the other type of steel with non oriented grain, made with a maximum of 3.25% of silicon, allows a better heat exchange behavior and a good permeability compared with steel containing more silicon.

## 4.1 Stator lamination material

Concerning stator laminations, the material must comply on a high value of magnetic saturation and low power losses to increase efficiency. Many manufacturers produces electrical steel with a percentage of silicon in order to narrows the hysteresis cycle and to increase resistivity reducing eddy currents. In this treatment reference is made on *Voestalpine Isovac* ®, according to the European standard EN 10027-1 which states rules for designating steels:



where:

- **M** stands for electrical steel
- **n n n** reporting specified losses in W/kg  $\times 100$
- **n n** is the thickness  $\times 100$
- **a** may be A if the steel is non oriented, D is a non alloy not completely annealed either E if is alloy not totally annealed

to reduce eddy currents losses the aim is to reducing material thickness, so the investigation is on a 0.35 mm thick, to understand the influence of materials on the motor performance the following analysis were conducted:

- M235-35A
- M250-35A
- M330-35A
- M350-50A

In light of what above discussed, increasing thickness involves in a rise of total losses with a consequent decrease of efficiency, as showed in the picture below:

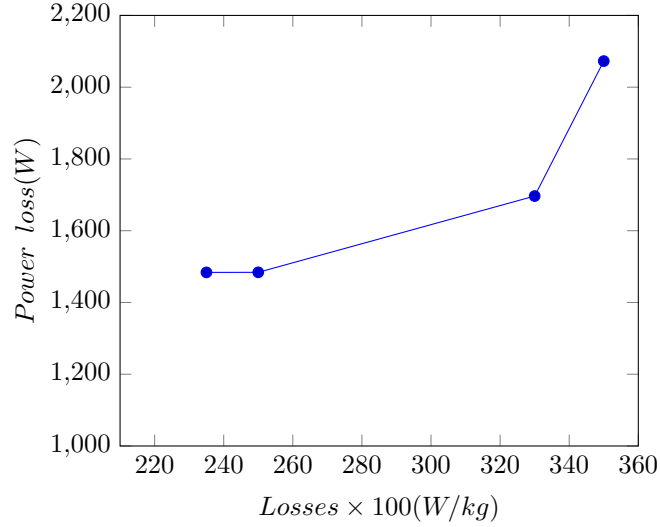


Figure 4.1.1: Lamination material comparison

Since materials need to be also economically sustainable, a good compromise is considered using M330-35A in which power losses are small and is thin enough to contain eddy current losses.

## 4.2 Rotor material

Concerning rotor's material, despite it is subjected to rotating magnetic fields produced by stator windings and coupled with the constant one of the permanent magnets, the absence of slip and the synchronous condition among the rotor and stator field not produce EMF and so eddy current i.e. phenomenon used in induction motor, so there is no particular necessity as in stator lamination. Hence, many manufacturers due to productive reasons uses solid rotor instead of a laminating one. Build the rotor with laminations is easy with small diameter, as the size grows appear constructive complications and to reduce inertia [19] would require also a material reduction in the region near the shaft, so to avoid this problem solid rotors are often made with a spider design to lighten it. These two possibilities affect the efficiency of the machine in such a way that use of solid rotor increases a lot eddy current losses, since they depends on the material thickness. To evaluate a solid rotor with dimension of motor designed in the previous chapter, it is considered as height of the rotor core the half of the length of magnet arc, condition which avoids rotor saturation:

$$\theta_m = \frac{2 \cdot \theta_e}{N_m} = 0.872 \text{ rad}$$

so

$$\text{arc} = \theta_m \cdot r_{rot} = 26.3 \text{ mm}$$

In the following table is shown quantitatively this difference:

As it was predicted, reduction in efficiency is due to the increase of eddy currents losses, instead, concerning hysteresis losses in the iron are zero when a solid rotor is adopted.

Data	M330-35A	C45
<i>Rotor iron losses</i>	2.867 W	50.35 W
<i>Eddy currents</i>	1.136 W	50.35 W
<i>Hysteresis</i>	1.731 W	0 W
<i>Total losses</i>	1706 W	1748 W
$\eta$	96.3 %	93.07 %

Table 4.1: Technical specifications

A finite element analysis using MotorCad simulation is done, in order to evaluate losses distribution in a laminated and solid rotor [20] in order, to show possible hotspots which could lead to demagnetization. Figures are both shaded with a jet color map  $[0 \div 302] \frac{W}{kg}$ .

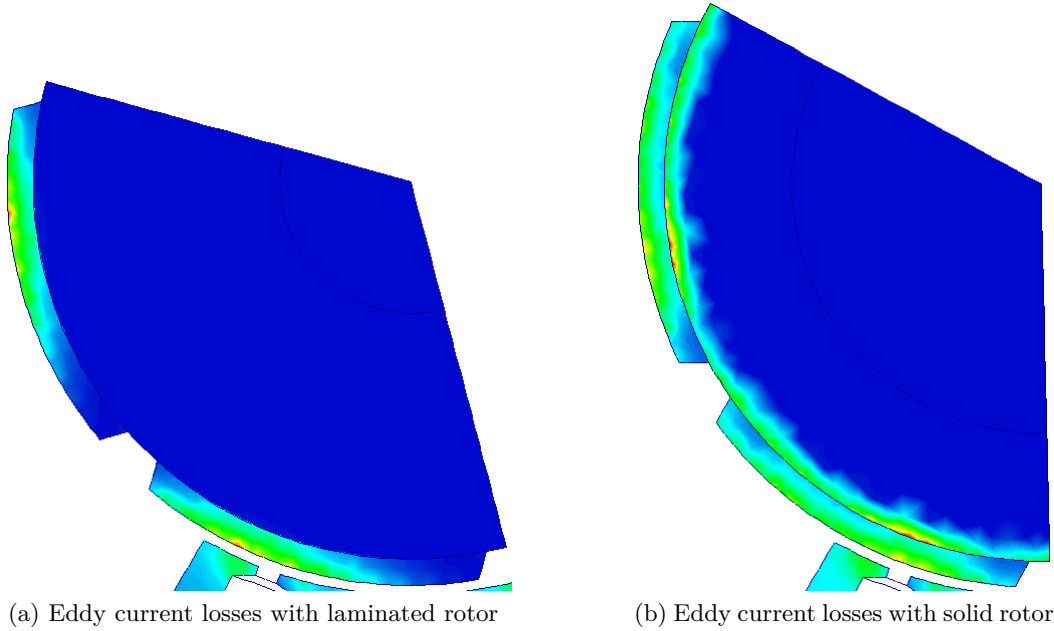


Figure 4.2.1: Power losses in rotor region with laminated and solid solution

At a glance, it is straightforward to see how the use of laminated rotor develops very low losses in particular in the magnets region, compared with a solid rotor one. The presence of great losses in the nearby region of magnets, make them prone to be thermal hot-spots and may lead in particular circumstances to unrecoverable demagnetizations.

## Chapter 5

# Electronic acquisition system for telemetry data

### 5.1 Telemetry data monitoring system

With the growing necessity of monitoring systems with the aim of reducing downtime, therefore also operating costs, prevent failures become crucial. Since every designer knows which are the parameters which identify issues to mechanical system, many methods to record these were developed, one of this, in this discussion is used an electronic modular platform to record CAN data coming from the electronic control units.

**CAN bus:** stands for *Controller Area Network*. It is a standard protocol to transmit data among different ECUs, made of two wires bus with a total characteristic impedance of  $120\Omega$  which determine the end of every bus. The data transmission can be synchronous, so with a clock time, or asynchronous with a starting bit. It could be of two types based on the **Baud rate**:

- High speed CANbus up to 1 Mbit/s
- Low speed CANbus up to 125 kbit/s

The speed is chosen in dependence of the cable length, since it is restricted by the speed of light, the message needs to reach the most remote node of the network and come back before the next message is sent. So the higher is the cable length, the lower needs to be the communication speed. The main feature of this protocol consists in a peer-to-peer communication: every component can communicate with each other and the message can follow different routes to reach the destination, this characteristic makes it so reliable, useful in fields such as automotive or aviation and so on. Considering a binary communication protocol carried by two wires, there are two possible states (High-Low): the main voltage of the line is 2.5V, if  $CANH = 3.5V$  while  $CANL = 1.5V$  so  $\Delta V = 2V$  a *recessive* bit "1" is transmitted, otherwise if  $CANH = CANL = 2.5V$  so  $\Delta V = 0V$  a *dominant* bit is sent. Taking into account high speed CAN bus, messages are made of:

**Start bit** identify starting of message

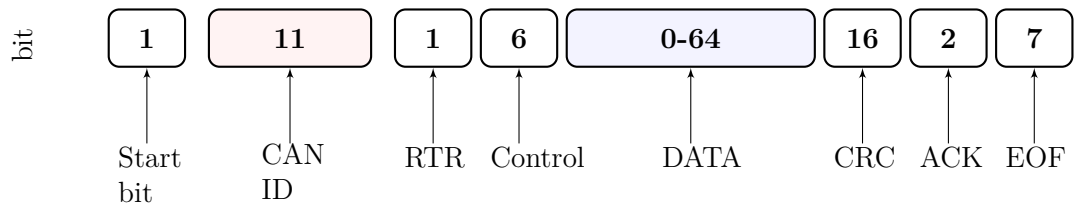


Figure 5.1.1: Base frame format of a CAN string

**CAN ID** set priority of messages

**RTR** Remote Transmission Request, when a dominant bit is transmitted (1) means that it has been requested by another node, specified by ID.

**Control** Defines data transmission

**DATA** String of data transmitted

**CRC** Cyclic redundancy check, makes a control on the data length transmitted

**ACK** Acknowledges, check if the destination node has successfully received message

**EOF** End of frame bits

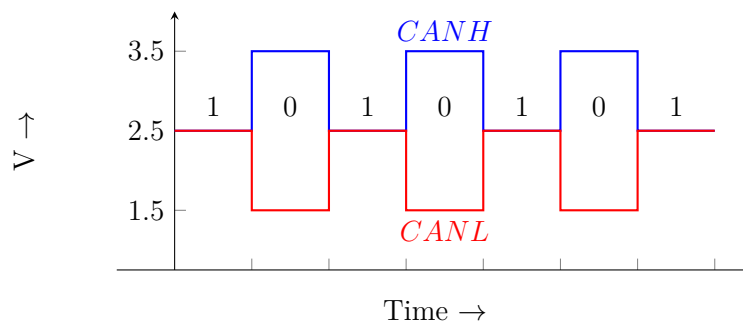
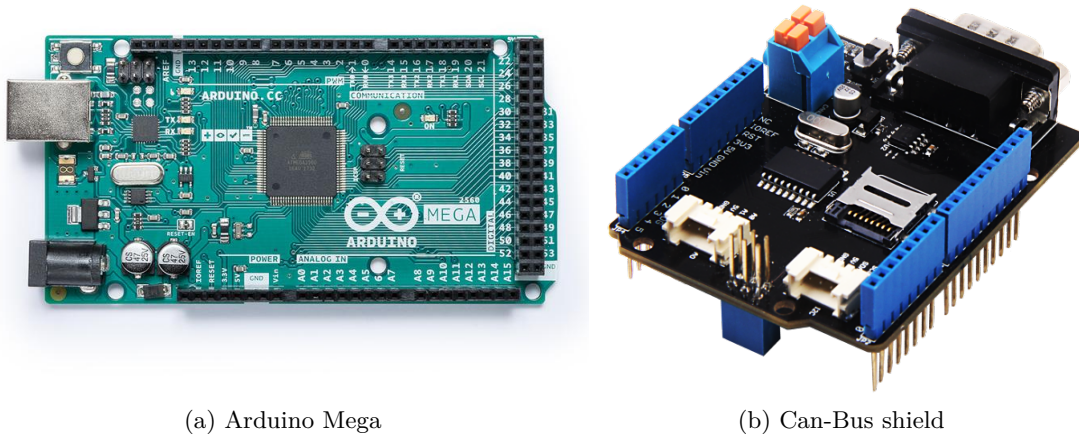


Figure 5.1.2: Voltage AND logic of the CAN bus

As an example, to translate CAN bus messages from hexadecimal to decimal transmitted following the J1939 or RS232 protocol, the offsets and scale factors are implemented. The Arduino platform used [21][22] in this work is composed by:

- Arduino Mega
- Arduino CAN-Bus shield v2
- Arduino IMU 9 axis motion sensor
- Arduino GPS shield



(a) Arduino Mega

(b) Can-Bus shield



(c) Arduino 9-axis motion

Figure 5.1.3: Arduino acquisition system

Arduino Mega is a micro controller board, on which is mounted the Arduino CAN-Bus shield, which tasks besides reading CAN H and CAN L messages, it writes on the micro SD data specified in the code to complete the system, an inertial measurement unit is mounted above the CAN shield, thanks to which has been possible to record data coming from 3-axis gyroscope, 3-axis accelerometer and magnetometer data which reads the gravity acceleration. The main feature of the Arduino IMU shield is the onboard Digital Motion Processor which allows a decoupling of the linear acceleration and components of gravity acceleration through a data fusion algorithm. In addition, a GPS module is mounted to record the path of the vehicle and allows the matching of every data to the position recorded in that moment. At the end, every string is written on a ".txt" file in the *μsd* card memory. A discussion about time of saving needs attention: there is a certain time delay depending by the bus speed, by the memory access time and write speed itself. Since each data has a difference frequency, e.g. GPS data updates every 1 sec, instead CAN

bus data has a frequency of 250Hz a lower saving time may leads to data losses, so there is a data repetition while others are updating. At the end, the bottleneck is represented by the writing stage, which minimum allowable time by  $\mu sd$  card is found with a period of 50 ms. Controller area network receive data from the drive and EPM about motor, battery and temperatures of drive and EPM themselves. In the table below are shown data acquired: In order to select properly messages passing through the network, by saving just messages

Data	Unit
Reference speed	rpm
Motor speed	rpm
Motor current	A
SOC	%
Battery current	A
Battery voltage	V
Motor temp	°C
Power temp	°C
Battery pack temp	°C
Internal temp	°C

Table 5.1: Drive CAN-Bus messages

Data	Unit
Output voltage	V
Battery current	A
Battery power	kW
Input voltage	V
12V battery voltage	V
12V battery current charge	A
Internal EPM temp	°C

Table 5.2: EPM CAN-Bus messages

shown in the tables 5.1 and 5.2 above, filters and masks are added in the Arduino sketch. A mask allows to select a precise number of bits and comparing therefore with the filter. In this way we are able to choose which messages save and which discard.

This system is mounted on board of a "Fiat Panda" electric prototype, in which the internal combustion engine has been replaced by an electric powertrain and in the trunk a battery pack is mounted which configuration consists in 192 cells connected in series, whose characteristics are shown in tables below:



Figure 5.1.4: Fiat Panda 2nd series

This vehicle has the characteristics shown in tab 5.3:

Data	Value	Unit
Power	43	kW
Battery capacity	16	kWh
Nominal voltage	640	V
Max speed	120	km/h
Average range	142	km

Table 5.3: Vehicle characteristics

Data	Value	Unit
$V_{nom}$	3.2	V
Capacity	25	Ah
Peak power $P_{max}$	48	kW
Cells $N$	192	—
Modules $N$	4	—
Cells $\times$ modules	48	—

Table 5.4: Battery cells characteristics

The acquisition platform is mounted on the vehicle by connecting it to 12V power system and to the CAN-Bus line. Then to read GPS data, the antenna is installed on the front of the vehicle windshield. In this paper a custom driving cycle is studied and recorded to analyze performance of the electric vehicle. In particular, this includes a mixed path: city, highway and hill, in order to identify a meaningful value for the energy consumption and to estimate battery life.

Data are analyzed with a Matlab script, in order to catch interesting data whereby draw conclusions about the electric motor behaviour, with particular reference to the thermal trend. In the script, data stored on the  $\mu SD$ -card are imported, translated from hexadecimal to decimal, then are scaled and with offset applied are ready to be post-processed. Finally, data are plotted to visualize information and catching functional anomalies or relevant working conditions.

## 5.2 Duty cycle definition

The working cycle[23] studied consists in a mixed route path, to test the vehicle in different conditions: urban, highway and uphill. To better understand the covered path a map showing the geographic data like altitude, latitude and longitude is shown in Fig.5.2.1 and Fig.5.2.2 :

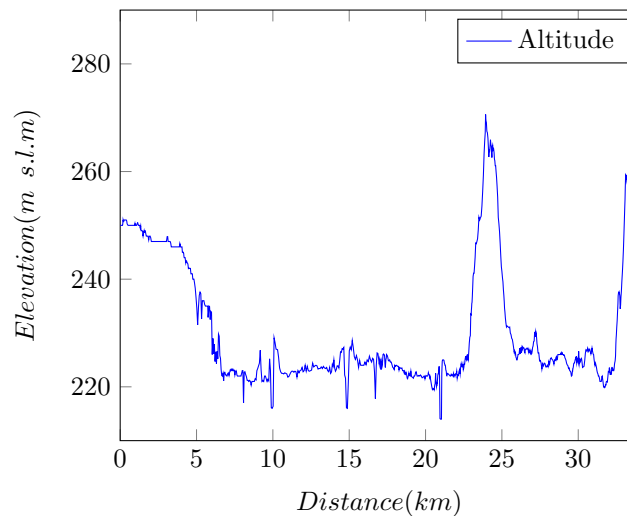


Figure 5.2.1: Altitude recorded by GPS

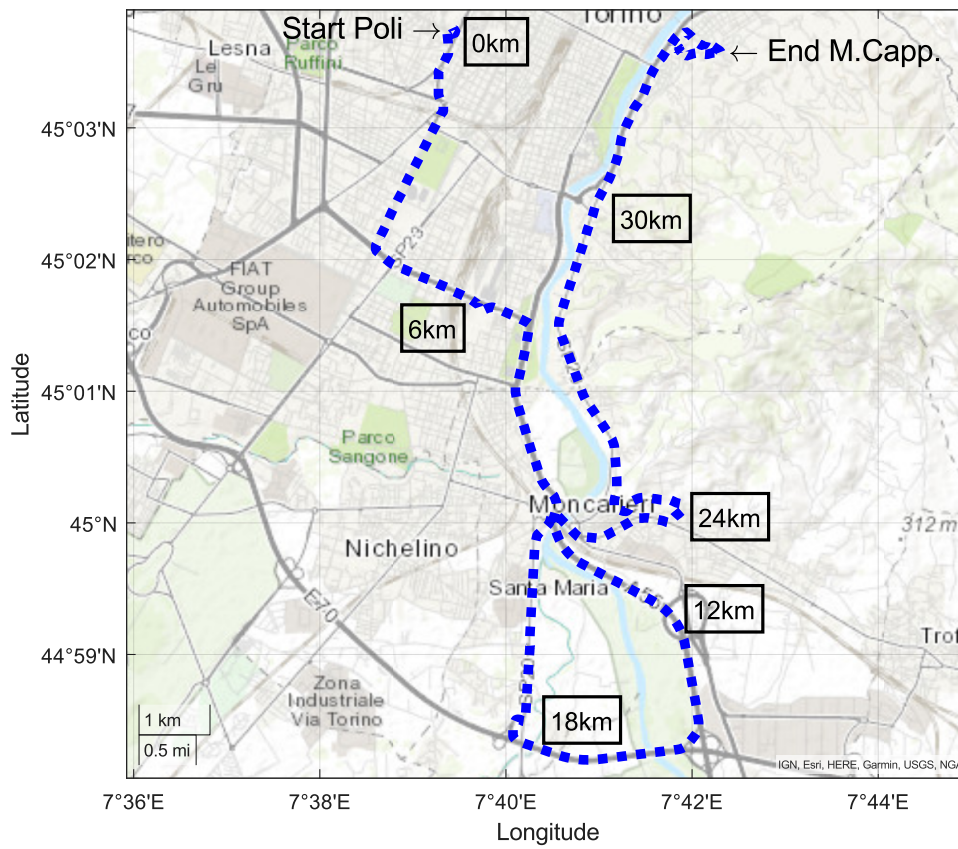


Figure 5.2.2: Driving cycle GPS path

The mixed cycle covered has the following properties:

- Space covered  $\simeq 34km$
- Difference in altitude  $\simeq 60m$
- Average speed  $\simeq 36km/h$
- Cycle time 60 *min*

In the following figure the power delivered to the motor is shown with color shades, to be specific: blue range points stand for regenerative braking, while red range color points indicate power absorption, instead with a different markers area is represented the slope change, in this way the power consumption can be correlated with the potential energy, so the recovered energy can be related with a brake nearby a traffic light either rather than along a downhill. After clarifying the cycle path, data analyzed are the ones that conduct

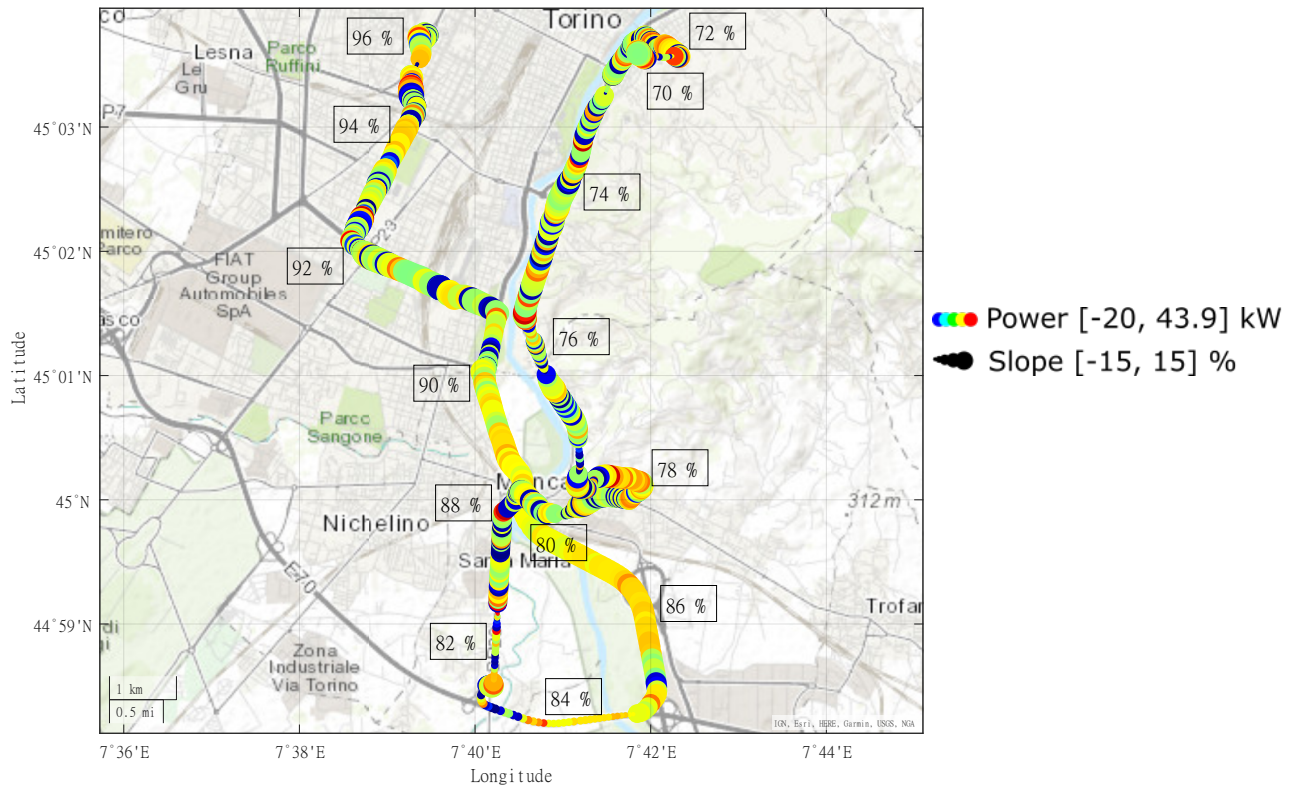


Figure 5.2.3: Driving cycle power and slope path

to the discussion about vehicle performances, in particular:

- Motor speed
- Battery current
- Motor power
- Motor current
- Motor temperature

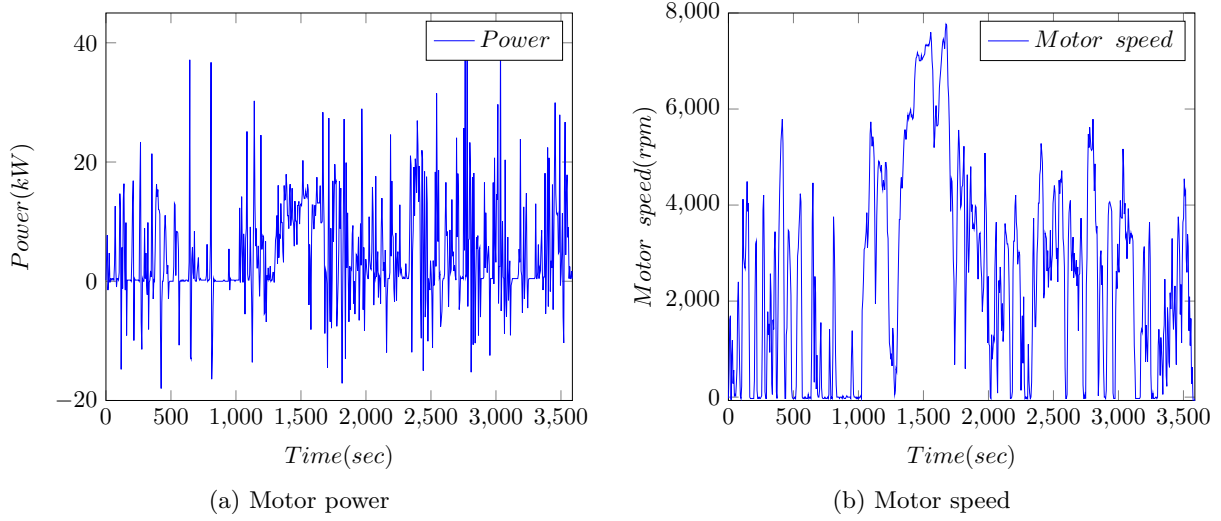


Figure 5.2.4: Fundamentals motor telemetry data

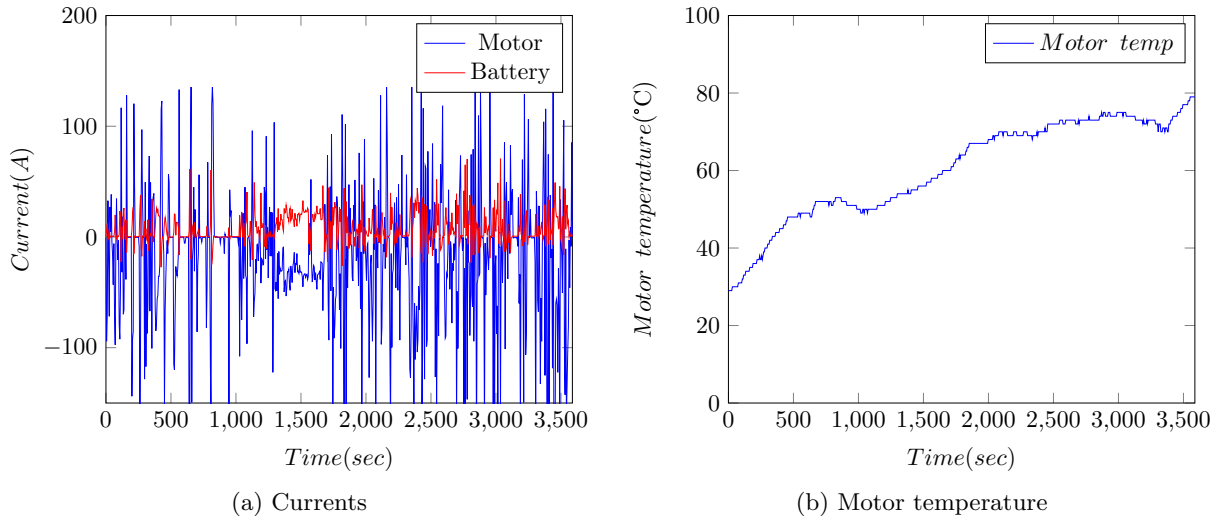


Figure 5.2.5: Internal motor data

From the previous graphs many considerations could be done. First of all about power, calculated as:

$$P = V_{batt} \cdot I_{batt} \quad (5.2.1)$$

so this is the upstream power and may be used to exploit consideration about the electrical transmission efficiency, by comparing Fig.5.2.4a with the downstream power of the shaft as later explained. Hence, in the figure 5.2.4b the pure motor shaft speed is represented, this is significant to identify, also without GPS data, the cycle position of the vehicle. The next one Fig.5.2.5a shows the health condition of the vehicle, in the sense that motor

currents and battery currents appear different. Since motor produces back electromotive force (BEMF) which works against the applied voltage, the current flowing through the winding is:

$$I_{motor} = \frac{V_{drive} - BackEMF}{WindingRes} \quad (5.2.2)$$

so this means that, considering the low values of motor winding resistance ( $\simeq 0.007$ ), a rise in motor speed makes  $I_{motor}$  closer to  $I_{battery}$ , as it can be seen in the middle period (highway path) where the Fig.5.2.4b reports high value of motor speed. From these considerations it is worthwhile that the electronics drive is responsible to keep motor currents under a certain limit, because with high value of currents are therefore generated high values of  $H$  that could lead to demagnetization. When such a phenomenon occurs, from this graph can be seen a huge gap among currents also at high speed, this means that magnets are permanently damaged and so they are no longer capable to produce EMF. This means that currents need to be controlled, this task is accomplished by applying a voltage just to overcome the winding resistance drop and the BEMF produced by the motor. Last graph 5.2.5b reports the motor temperature as a function of time, this is also an important parameter to control and avoid motor faults like demagnetization, moreover dielectric strength[24] decreases with increase in temperature, loosing the insulation resistance and become conductors. As will be shown in the later chapter, it is understood how the thermal design is a critical issue in the motor project, since it allows the proper motor performance.

### 5.3 Post processing data analysis

In order to process data collected from the vehicle CAN-Bus, a Matlab script is used to translate strings from hexadecimal to decimal and organize them as it has been written. The following data are shown and every group allows to make considerations about vehicle status.

In a macroscopic view the overall performance is taken into account:

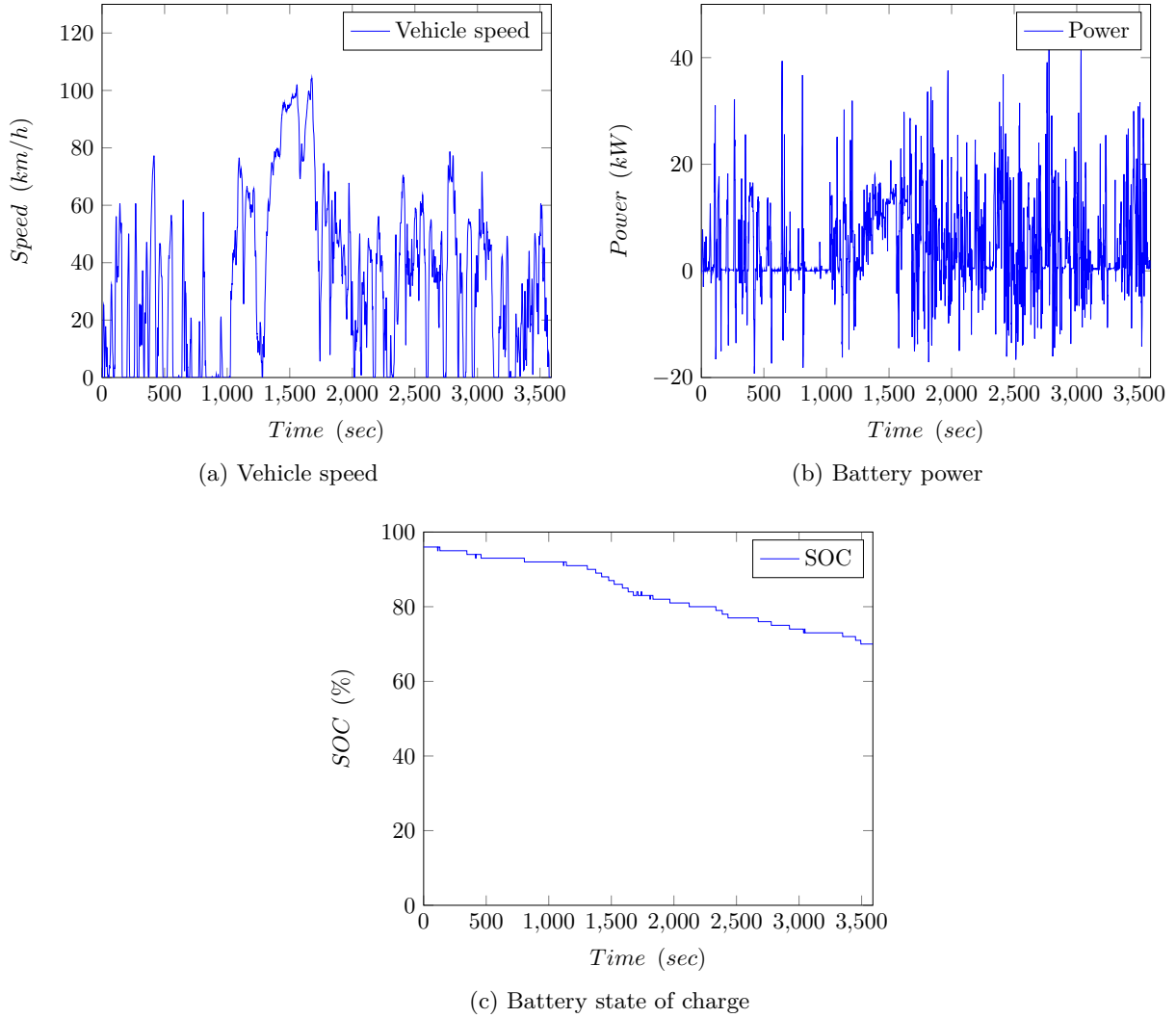


Figure 5.3.1: Vehicle telemetry data

In the figure 5.3.1a is reported the exact vehicle velocity, read from resolver signal, converted with transmission ratio  $\tau$  of the gearbox as angular velocity of wheels and finally transformed in velocity with the radius. The graph 5.3.1b is the same aforementioned, repeated in order to compare the SOC decrement. Regarding the figure 5.3.1c is shown the decrease of energy stored in the battery pack, this graph allows to find the motor electric energy consumption along the cycle either with the increases in the state of charge level is possible to evaluate recovered energy:

$$E_{motor} = \Delta SOC \cdot C_{battery} = 4160Wh \quad (5.3.1)$$

With reference to figure 5.3.1a in which the exact velocity is reported, allows further consideration about the GPS accuracy [25]. In particular since the precision depends on

many factor, such as presence of buildings, radio interference, atmospheric conditions and number of satellites effectively connected. In the following pictures are shown the two speeds recorded:

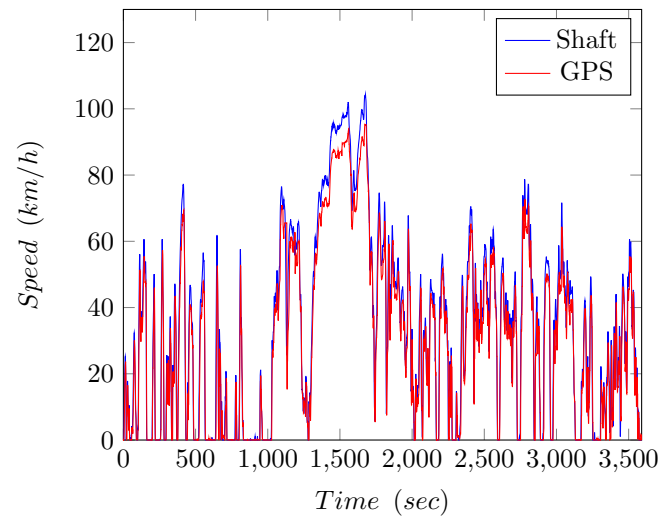


Figure 5.3.2: Shaft speed VS GPS telemetry speed

To complete the overall description of the components monitored within the vehicle by means of telemetry data acquisition, the attention is focused on battery pack. The wide spread of battery electric vehicles is hampered by the increasingly higher capacity and power requested by the customers with respect to the ones which batteries can give. Many studies[26] conduct analysis about the behaviour of a battery pack in a particular application, with the aim to find the best configuration which satisfy the requested load conditions. In the pictures below are shown characteristic data collected from the battery pack, voltage, current and operating temperature: This type of cells,  $LiFePO_4$ , have an

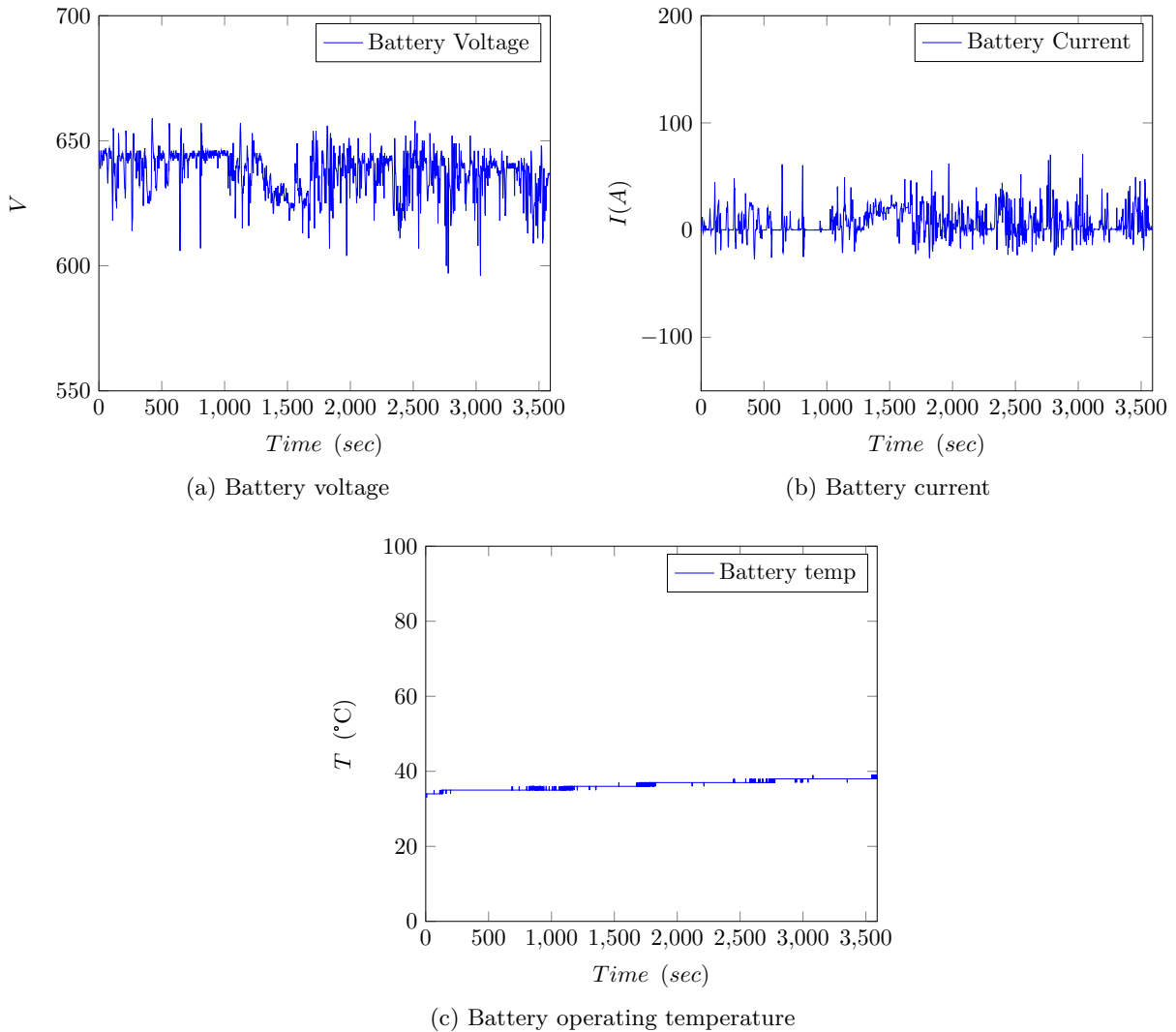


Figure 5.3.3: Battery pack monitoring data

operating voltage between  $2.7V \div 3.65V$ . These values are the cut-off voltage controlled by the BMS during charge and discharge cycles. By knowing the cells configuration (192s)

the overall voltage of the battery pack is obtainable. In the same way, by knowing the cell capacity from Tab.5.4, the BMS needs to control the charge and discharge C-rate current, by the manufacturer's sheet it is recommended a  $1C$  as nominal charge and  $3C$  nominal discharge current. Hence, these graph are useful to monitor the electronics operation and the operating temperature which has to remain in a range of  $-20^{\circ}\text{C} \div 55^{\circ}\text{C}$ .

## 5.4 Duty cycle simulation

Ones data coming from the motor are collected and examined through a first skim, for instance there could be necessary to have further information about the working cycle in order to solve motor fault or suspected conditions. In this step, the designed motor with MotorCad and telemetry data are coupled, in particular a duty cycle is filled out. The definition may be done in different ways:

- Torque - Speed
- Current - Speed
- Vehicle Speed

In the third case precise vehicle characteristics are needed to make the model, like rolling resistance, frontal area, drag coefficient, making able the software to calculate every loss contribution. In this case, since the interest is focused on the electric motor characteristic, the duty cycle is defined through the current. From telemetry data the total motor current is resorted, without the decoupling in  $I_d$  and  $I_q$ , in this case it is assumed that  $I_d = 0$ ,  $I_q = I$ . In order to optimize the computation time, data are represented with a time step in a way to cover a time of 1 sec between two consecutive points. Firstly, the power directly produced by the motor is shown in the figure below: By comparing this peaks data fig.5.4.1 with

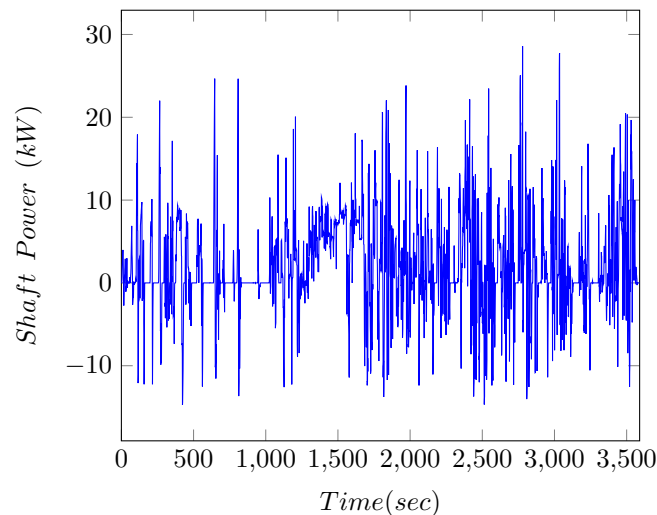


Figure 5.4.1: Shaft power calculated by MotorCad

the ones reported in fig. 5.2.4a, is fairly straightforward that these values are lower than

the others. The reason, as stated above, is that the first power is the upstream power, instead the figure reports the downstream one. Between them there is the efficiency of energy transmission among:

1. Power electronics
2. EPM
3. High voltage cables

It is estimated that the global efficiency calculated as:

$$\eta_g = \eta_{Drive} \cdot \eta_{EPM} \cdot \eta_{Cables} \cdot \eta_{Motor} = \frac{P_{shaft}}{P_{battery}} \simeq 73\% \quad (5.4.1)$$

This simulation can be validated by calculating the downstream power from the motor, beginning from the acquired currents, with the  $K_t$  is find the torque and with the speed is obtained the shaft power. Further considerations can be done by looking to the Duty cycle analysis data: MotorCad Lab-section analysis allows to control each time step of the driving

Data	Value	Unit
Average efficiency	88.6	%
Electrical input energy	3249	Wh
Shaft motoring energy	3096	Wh
Electrical output recovered energy	695	Wh
Shaft generating energy	728	Wh
Total loss	186	Wh
Motoring operation	75.7	%
Generating operation	24.3	%

Table 5.5: Duty cycle analysis

cycle, in the sense that if any kind of anomalies would arise, every operating parameter is well known. As it is shown in the figure below, with the calculation of efficiency map and by superimposing every point of the duty cycle, considerations about the motor size and the proper design for the application can be made. Map in the figure 5.4.2 shows the working condition of the motor and allows a design review, in order to accomplish the power demand. As can be seen, just a little amount of the total points are in the high efficiency region as the combination of torque and speed. The other part are in a lower efficiency area, this is the reason of the average efficiency reported in 5.5. Most of the working points are settled in the low efficiency region of the map, with a combination of low torque and high speed, this suggests that a further review should move points through high efficiency improving losses and energy consumption, this could be made by use of a different control strategy like a variable phase angle instead a constant one fixed to zero. One of the fundamental outputs data are the losses produced in each motor part. Calculation of each loss contribution is useful in the choice of materials, in the figures 5.4.3 is shown the influence of the lamination thickness on an extended driving cycle. As it can be seen, an increase in thickness involves strong differences, a decrease in the efficiency

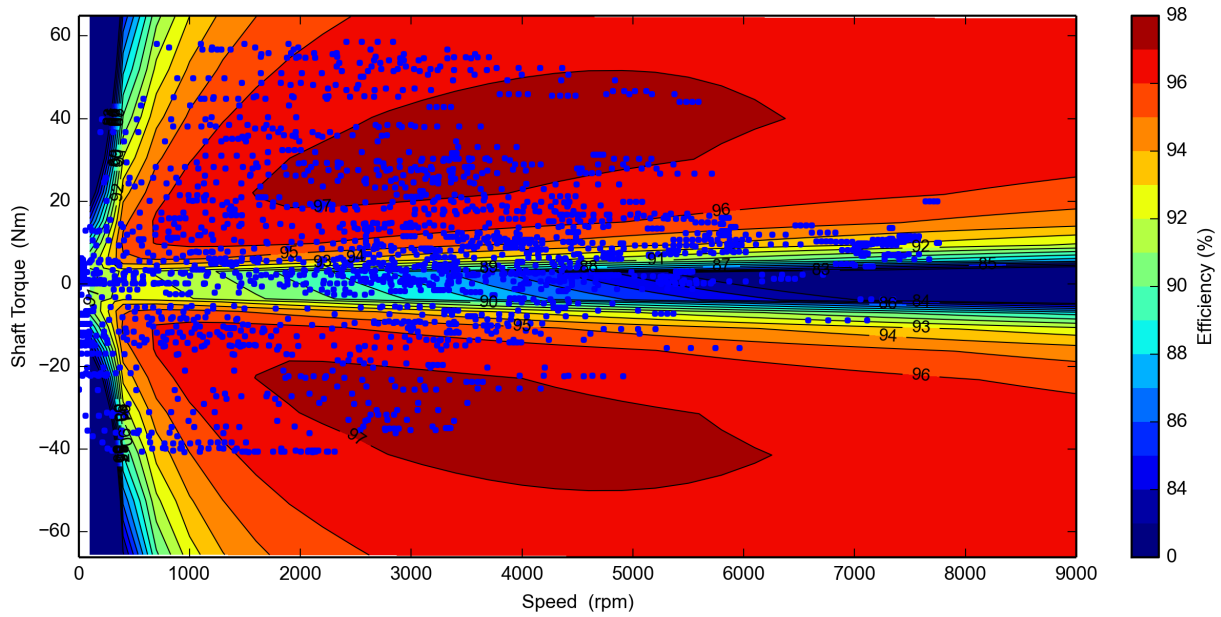


Figure 5.4.2: Efficiency map with drive cycle

but a save in costs. For a vehicle application these aspects need to be evaluated to find a compromise between costs and benefit. Losses results constitute the input data used for

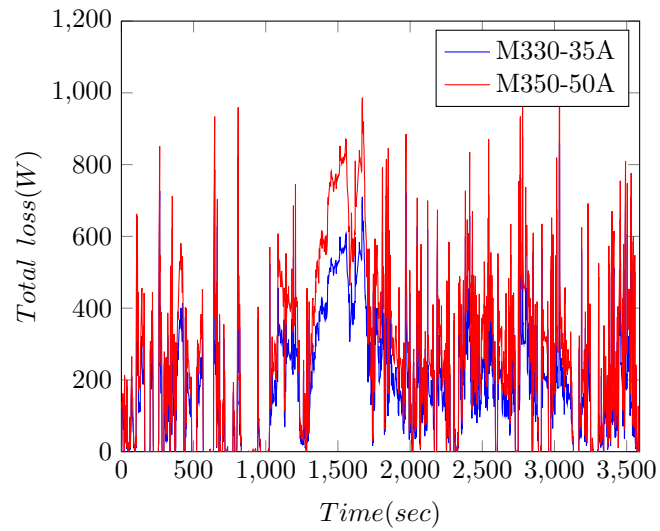


Figure 5.4.3: Total losses comparison with electrical steels M330-35A and M350-50A

the thermal simulations, an increase in losses falls on an increase in heat produced by the motor and so will determine a different thermal design approach. In this analysis are taken

into account the worst case to develop thermal design, by using M350-50A laminations.

## 5.5 Mechanical stress analysis

Since the rotor of electric machines is subjected to high rotational speeds, it is called in every moment to withstand centrifugal forces. In this configuration, with surface mounted magnets, basically glued on the rotor perimeter, the centrifugal stress at which they are subjected may lead to detachment, for this reason each manufacturer shall adopt a different solution to increase the radial stiffness. Dealing with this case two solutions could be adopted:

- Harmonic wire rotor banding
- Magnet retention sleeves

The model uses the following mechanical properties for materials: The solution shows

Material	Young's modulus	Poisson's modulus	Yield stress
M350-50A	20000 MPa	0.3	305 MPa
N30UH	16000 MPa	0.24	30 MPa
Carbon fiber sleeve[27]	70000 MPa	0.1	600 MPa

Table 5.6: Mechanical properties of materials used in the model

the Von Mises stresses calculated on the rotor with a rotational speed of 9000rpm. With

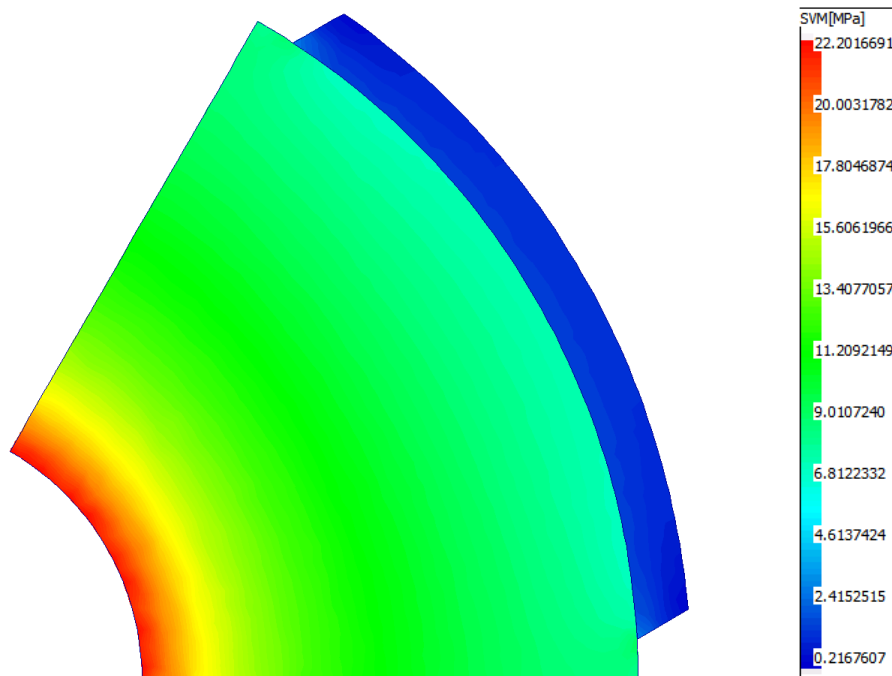


Figure 5.5.1: Rotor stress FEM analysis

reference to the fig.5.5.1, even if from the color shown it seems that the rotor is in critical condition, taking into account the Yield stress reported in the tab.5.6, there is a coefficient of **13** with respect to the maximum stress. The last important mechanical analysis consists in the evaluation of displacement. Since the rotor is subjected to the cylindrical tolerances prescribed in production stage and it is separated just from 1.5mm of air gap from the stator teeth, when it runs at high revolution speed it is inevitably subjected to deformations that try to change its shape. With this analysis the shape can be seen and also is quantitatively analyzed the stiffness. In the fig.5.5.2 the magnitude of displacement is of the order of

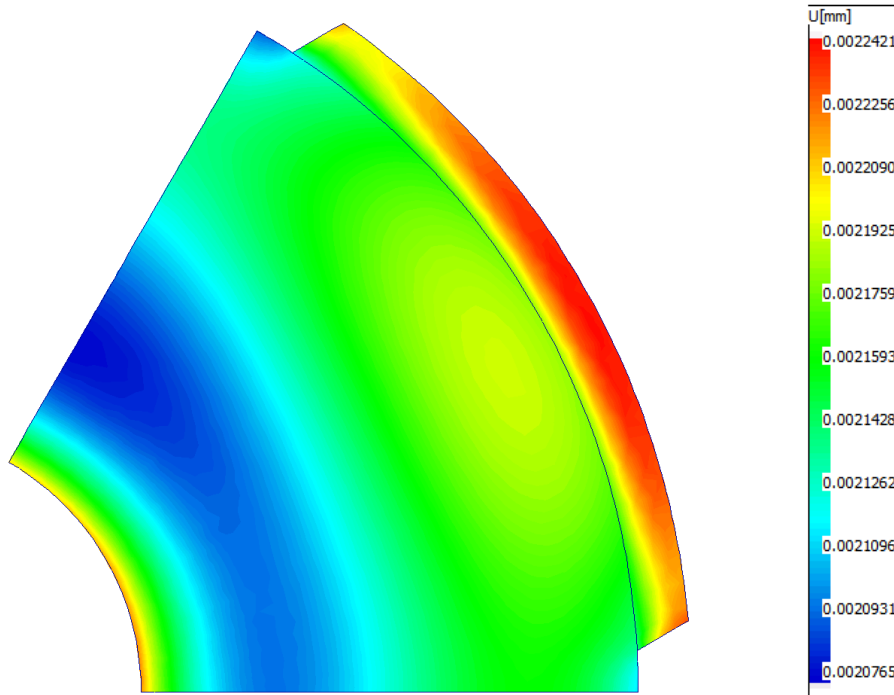


Figure 5.5.2: Rotor total displacement FEM analysis

microns (maximum of  $2\mu m$ ), which not represents a critical issue.



# Chapter 6

## Thermal design of a PMSM

### 6.1 General overview

Thermal design of a permanent magnets electric motor is a crucial point which needs a particular attention, since a proper heat management determines the development of the prescribed performance. There are several ways to cool motor:

- Housing water jacket
- Rotor water cooling
- Spray cooling
- Slot water cooling
- Ventilated

The simplest way to cool the motor is with air, through natural convection, by realizing fins on the external surface of the housing. This method assumes that all the heat generated within the motor is well conducted to the external surface, this goal is obtained using materials with a good thermal conductivity  $\lambda$ , either increasing this parameter with high conductivity materials like resins. Therefore, use of a liquid cooling is a better choice thanks to the higher specific heat of cooling fluids, which means that is required less mass compared with air, to obtain the same heat absorption. To introduce liquid cooling is worthwhile understand which laws govern heat transfer, in this way the thermal design becomes easier. Starting from the dimensionless numbers[28]:

$$Re = \frac{\rho u L}{\mu} \quad (6.1.1)$$

$$Pr = \frac{c_p \mu}{k} \quad (6.1.2)$$

$$Nu = 0.664 Re^{1/2} Pr^{1/3} = \frac{hd}{k} \quad (6.1.3)$$

In the Eq.6.1.1 is described the ratio between inertial and viscous forces, within a fluid subjected to internal movement due to velocity. The Eq.6.1.2 introduces the properties of

a fluid in heat conduction, is calculated as the ratio of momentum to thermal diffusivity, in other words defines the dominant heat transfer among convection ( $Pr \gg 1$ ) and conduction ( $Pr \ll 1$ ). Finally with Nusselt in eq.6.1.3 is the ratio of convective to conductive heat transfer at a boundary layer. To have more convection a larger Nusselt number is needed, which implies a turbulent flow ( $Re > 5000$ ). With this brief discussion, it can be understood that a housing water jacket needs to be designed in a way to obtain certain results, ensuring so a good heat transfer. Other cooling strategies may be adopted, but the complexity introduced in the project are not negligible. For example a rotor water cooling [29] has the leaks problem, the fluid passing through the shaft, which turns at high revolution speeds, it needs strong seals to avoid fluid return. Slot water cooling has the requirement that heat pipes have to pass through stator slots, where are placed windings: this is on one hand a smart way to cool, because the heat is removed where it is produced, but in faults cases there could be several complications considering the high currents flowing in the wires. Furthermore, the space requested for heat pipes within the slot reduces the available space for the windings turns, otherwise the area needs to be increased, reducing so the total number possible with the considered diameter.

## 6.2 Housing water jacket design

In this section, to understand the temperature distribution within the motor in each duty cycle point, many hypothesis were stated about its design with the goal to match the known temperature reading in the NTC sensor region. Housing water jacket is composed by two parts: the first is the outer wall, directly in contact with stator laminations and mounted with an interference of  $\simeq 0.2mm$ , in order to obtain a good surface contact and ensure a good conduction heat transfer. The internal shell is made with high conductivity Aluminum alloy, while the external surface is made of stainless steel, since it has a structural assignment. In the external shell, are milled the channels, with dimensions[30] reported in the Tab.6.1 and shown in the fig.6.1 below. Regarding the fluid, a mixture of water and

Data	Unit	Value
WJ channel - lam	6	mm
WJ channel height	4	mm
WJ channel width	33	mm
WJ channel spacing	25	mm

Table 6.1: Water jacket dimensions

ethylene glycol (50-50%) is chosen, the presence of glycol is essential for antifreeze and to increase the boiling point temperature. On the other side a decrease in specific heat and in kinematic viscosity, reduces Reynolds number with a consequence reduction in convection heat exchange. With a fluid volume flow rate of  $10l/min$  the following properties are achieved and reported in Tab.6.2:

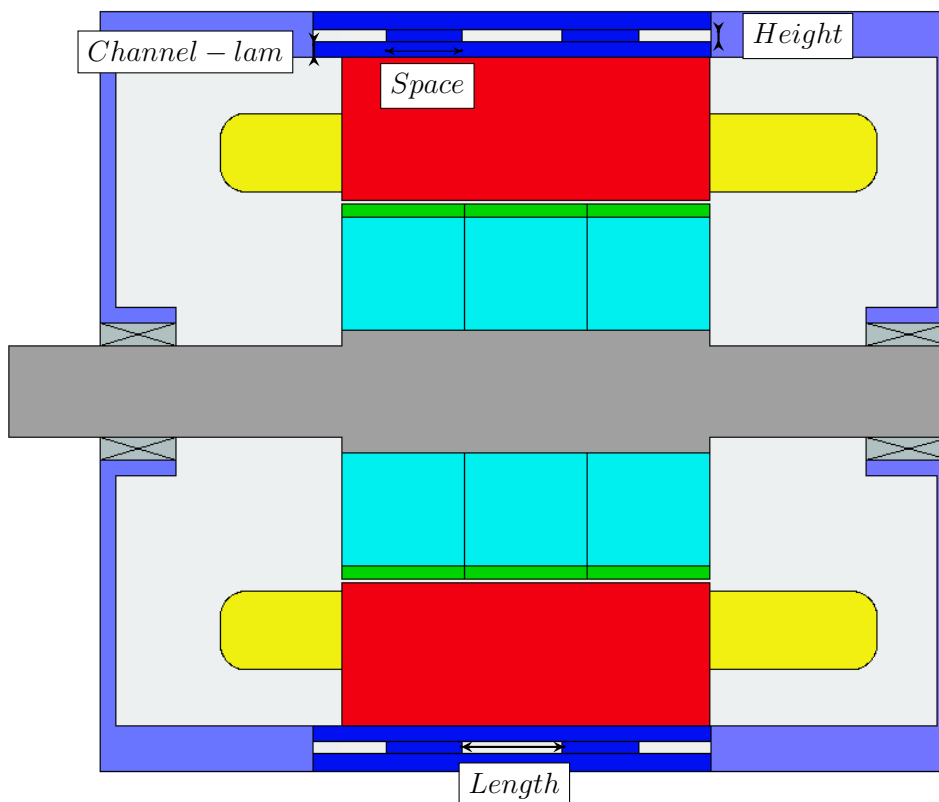


Figure 6.2.1: Motor water jacket drawing dimensions

Data	Unit	Value
Cross section area	132	$mm^2$
Length	2010	mm
$Re$	6018	–
$Pr$	20.2	–
$h$	3962	$\frac{W}{m^2 \cdot ^\circ C}$

Table 6.2: Fluid characteristic properties

### 6.3 Duty cycle thermal simulation

The evaluation and understanding about causes of critical faults are possible with the analysis in duty cycle. Starting from the lab losses 5.4.3, considered as inputs of the thermal simulation, the temperature in each interesting node for each analyzed point can be predicted. The experimental data acquired fig.5.2.5b show the unreached of a thermal equilibrium, for the time considered there is a rise in correspondence of each power demand, as can be seen with reference to Fig.5.2.4a. In this condition the heat generated inside the motor is not completely transferred to the fluid, the remaining part contributes to increase



relatively short motor the distribution is anything but homogeneous: in the center there is a heat build-up, since while the external rows of magnets are with a side in communication with the air, other than the upper part facing in the air gap, so the magnets can be cooled with convection along an extended area. The central row is in touch side by side with other magnets, so the heat is transferred mainly with conduction, except for the upper part facing in the thin air gap. As can be seen by the color blending, there are about  $10^{\circ}\text{C}$  of temperature difference from a row to the other and a difference of  $\simeq 35^{\circ}\text{C}$  from the sensor's temperature reading, furthermore considering that these magnets are N30UH with a maximum operating temperature of  $180^{\circ}\text{C}$ , at which irreversible demagnetization occurs, to monitor properly the health state of the motor are necessary more than one sensor on the external slots, because that position doesn't evidence the internal state. The

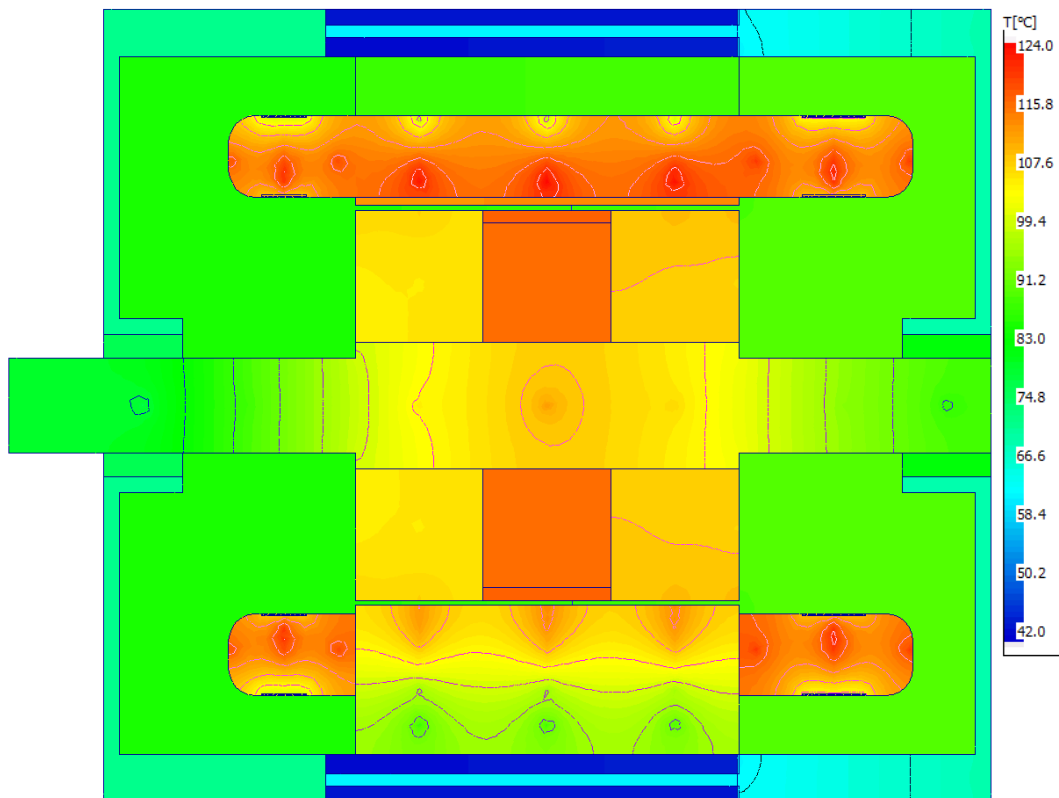


Figure 6.3.2: FEM axial temperature distribution

duty cycle transient simulation is performed considering three steps, to avoid the model of heat exchanger, of which data are unavailable. In each step the temperature of the fluid is increased, by simulating the rise in temperature of the real cooling system and the next simulation begins from the last temperature of the previous one. Setup of thermal simulation requires the setting on the inlet fluid temperature, since this data is not monitored from any sensor, but knowing the cooling configuration: in series are disposed first **drive unit** and then **electric motor**. So with the sensor information from the power electronics, solving the thermal problem for each point is found the temperature outlet which corresponds to the motor input. To obtain the model is assumed an efficiency of the electronics of  $\eta = 93\%$

and the losses are estimated from the power flows in.

$$P_w = I_{battery} \cdot V_{battery} \cdot (1 - \eta) \quad (6.3.1)$$

Power losses corresponds to the thermal power  $\Phi_w$ , in addition, since the drive temperature is known, with the calculation below the driver inlet temperature is obtained:

$$T_1 = T_2 - \frac{\Phi_w}{\dot{m}c_p} \quad (6.3.2)$$

in the graph is shown the results. Since the power involved is quite low, also the losses are

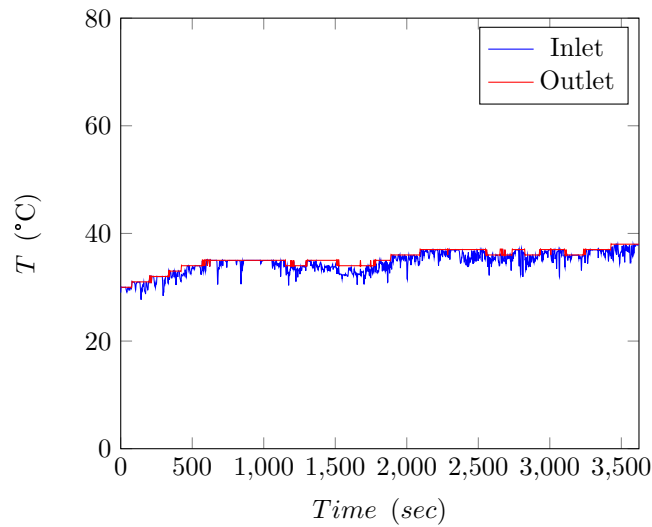


Figure 6.3.3: Inlet and outlet drive system temperatures

low. The approximation of a fixed inlet temperature of 40°C is reasonable.

## 6.4 Demagnetization analysis

Sintered NdFeB magnets are subjected to irreversible demagnetization[31] starting from temperature of 120°C, many causes can lead to this fault: i.e. short circuits or wrong thermal management. In this section the worse condition verified in the previous duty cycle is analyzed and a safety coefficient is found in order to evaluate how far the magnets are from fault condition. When a magnet is subjected to an external magnetic field, its behavior is dictated by the hysteresis cycle and its working point moves along a curve called *recoil line*[32] parametrized with the temperature. In correspondence of the maximum temperature (for N30UH 180°C), the lines show a knee at which irreversible demagnetization occurs. Instead for temperatures lower than the maximum, the knee is located to negative values both of  $B$  and  $H$ . The phenomenon takes place in a sense that the remaining value of magnetic field density  $B_r$  is reduced to a value in which the magnet is not able anymore to produce BEMF. Demagnetization[33] may occurs with a coupled effect both of impulsive currents and high temperatures, considering that heat is generated mainly in the coils and another part in laminations due to eddy currents losses. To describe the concept is introduced a magnetic equivalent [15] in Fig.6.4.1: As it can be seen the flux from the

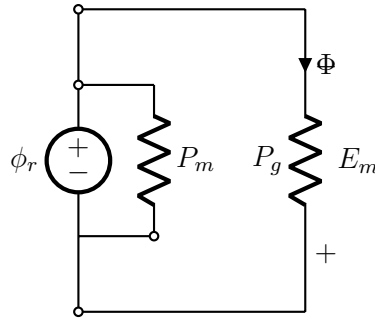


Figure 6.4.1: Magnetic model

magnet passes through the air gap and is filtered by their own permeability, as the balance of the fluxes states:

$$B_g A_g = B_m A_m \quad (6.4.1)$$

and so:

$$B_g = B_m \frac{A_m}{A_g} = B_m C_\Phi \quad (6.4.2)$$

where  $C_\Phi$  is denoted as *Flux concentration factor*, if  $A_m > A_g$  the flux density in the air gap is higher then the magnets one. This could lead to unsafe condition, so to ensure proper operation the magnet length must be greater then the air gap length. In the figure below is reported the curves for this type of material, and is evidenced the worse condition point found looking to the motor currents graph fig.5.2.5a. whose condition is shown in the tab.6.3 below: Starting from these data, to obtain the magnets working point, a magnetic simulation is needed. This point is found by a line whose slope is given by the *Permeance coefficient*  $P_c$ . Considering that:

$$B_m = \frac{\Phi}{A_m} \quad (6.4.3)$$

Data	Unit	Value
n	2090	<i>rpm</i>
Torque	58.7	<i>Nm</i>
$I_{Peak}$	274.3	<i>A</i>
Power	25	<i>kW</i>
T	70	$^{\circ}\text{C}$
Loss	635	<i>W</i>

Table 6.3: Critical working point

$$H_m = \frac{E_m}{l_m} \quad (6.4.4)$$

$$P_c = \frac{-B_m}{\mu_0 H_m} = \frac{l_m}{g} \frac{1}{C_{\Phi}} \quad (6.4.5)$$

The electromagnetic FEM simulation, with input data listed in the tab.6.3, shows a critical point in which the flux density  $B$  and magnetic field  $H$  are intensified as shown in the following figure: The magnet is no subjected to a uniform field, but it is shaded along the

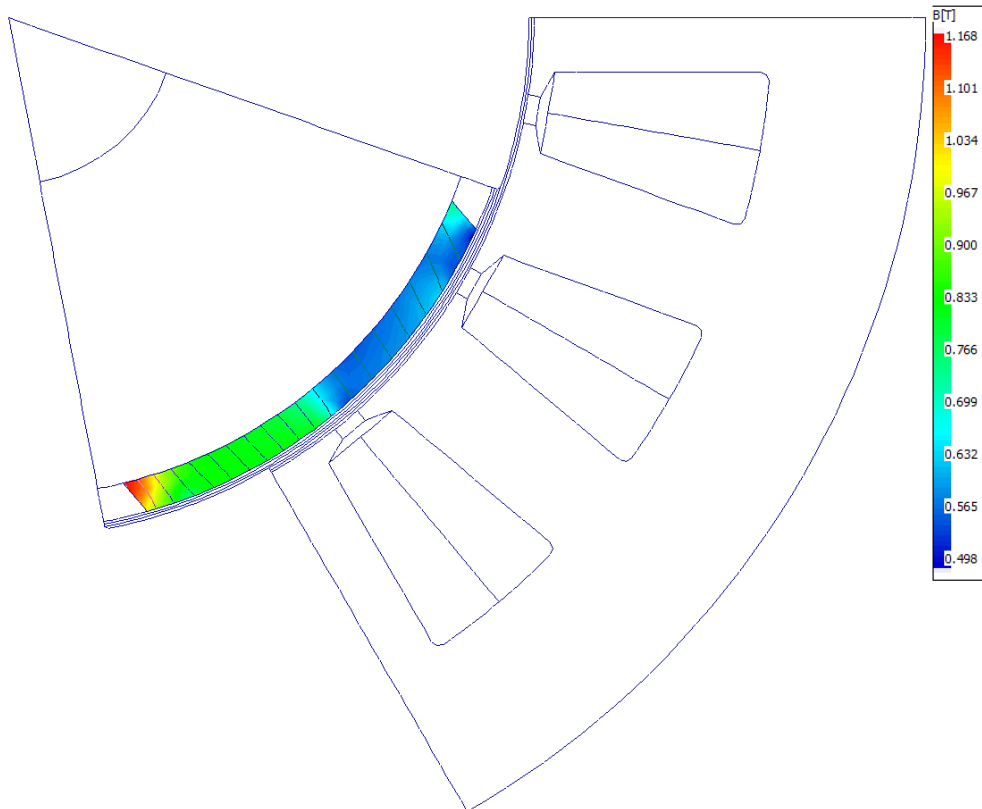


Figure 6.4.2: Magnets FEA analysis on critical load

length and sharper in a particular area. The  $B$  remanence at this temperature is evaluated by the demagnetization curve. When the magnet is subjected to a field produced by the windings currents, a coupling between two fluxes occurs: since half part (blue zone in Fig.6.4.2) of the magnets has the opposite field with respect to the one produced by the currents, fields interact subtracting each others and the resulting  $B$  is weaker. On the other part (green zone in Fig.6.4.2) there is a summation, for this reason, in certain areas the magnetic flux density is even higher than the remanence  $B_r$  at the operating temperature. The same considerations could be done about the  $H$  evaluation. Thanks to this simulation are found the specific results and the calculation of  $P_c$  with the formula 6.4.5 : The last consideration of this chapter concerns the assessment of a safety factor, a simple

Data	Unit	Value
B	0.498	$T$
H	441.7	$kA/m$
$P_c$	0.9	–

Table 6.4: Magnetic results at critical working point

value that describes the gap from fault condition. This value is calculated taking into account the properties related to the selected demagnetization curve shown in fig.6.4.3 at the operating temperature given in tab.6.3. From the material datasheet  $B_{knee}$  and coercive field  $H_c$  are extracted as reports the tab.6.5 below: Since the flux density depends on the

Data	Unit	Value
B	1.057	$rpm$
$H_{knee}$	-1430	$kA/m$
$H_c$	-1510	$kA/m$

Table 6.5: Magnetic results at critical working point

material permeability  $\mu_r$ , concerning the calculation of  $SF$  is considered more suitable use of the value of magnetic field  $H$ . In this way two coefficients can be found: one concerns the incipient of demagnetization at which the magnets doesn't recoil anymore along the demagnetization line, starting to loose  $B_r$ , the other one describes distance from the total demagnetization ( $H_c$  field).

$$CS_{demag} = \frac{H}{H_{knee}} = 3.2 \quad (6.4.6)$$

$$CS_{coercive} = \frac{H}{H_c} = 3.4 \quad (6.4.7)$$

The safety factors suggest that the magnets are working in a safe condition in the most loaded point of the cycle.

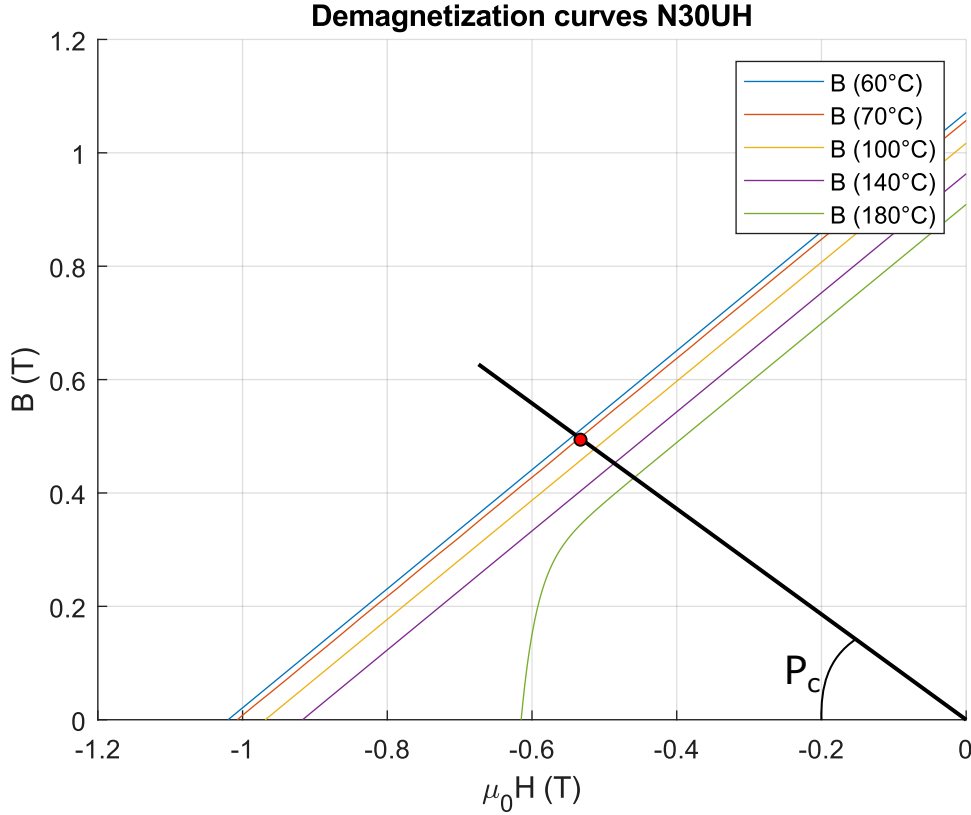


Figure 6.4.3: Demagnetization curve of magnets N30UH

## 6.5 Thermal design review

Considering that the temperature shown in the graph 5.2.5b are not critical for the motor safety as widely discussed in the figure 6.3.1 and controlled with the demagnetization analysis in the previous section, the motor temperature curve trend highlights that there is no thermal equilibrium. By comparing the graph temperature with the motor power, is noticeable that in each power demand the temperature increases. This behavior suggests that the heat generated inside the motor is no transferred by the fluid flowing in the water jacket ducts. Furthermore, the fig.6.3.3 well represents the heat exchanger outlet temperature, which corresponds to the one found at driver inlet. All this considerations allow us to understand that the water is well cooled by the vehicle’s heat exchanger, but nevertheless the motor continues to warm. Hence, it was deemed appropriate to design a custom cooling method that allows a proper functioning of the coolant loop. To increase the heat exchanging may be adopted different solutions, but each one has the objective to increase the  $h$  convective heat transfer coefficient. Looking to the parameters on which  $h$  depends, the first attempt is to increase  $Re$  (eq.6.1.1), by changing the fluid choosing a less viscous one, either increase velocity in the ducts. Changing the fluid properties also affect  $Pr$  coefficient (6.1.2). These first adjustments may increase the heat exchange, but in many cases the problem is not to be sought in the fluid, rather in the materials used.

Since the heat problem could be modeled with an electric equivalent (heat is the current and difference in temperature is the voltage):

$$R_{elec} = \frac{V}{I} \iff \frac{\Delta T}{q} \quad (6.5.1)$$

the only parameter exchangeable is the material resistance just by changing material or by using arrangements to reduce the resistance. This reviewed configuration explores a fully covered ducts along the axial direction closer to the stator lamination in a spiral groove. The method adopted follows the design of a shorter front and rear end caps, by increasing the dissipation area and ensuring the structural supports. Furthermore, all the housing is made with aluminum alloy, which increases the thermal conductivity and allows also dissipation with the ambient. In the picture 6.5.1 below is shown the design and the following graph shows the temperature simulation along the driving cycle. From this latter

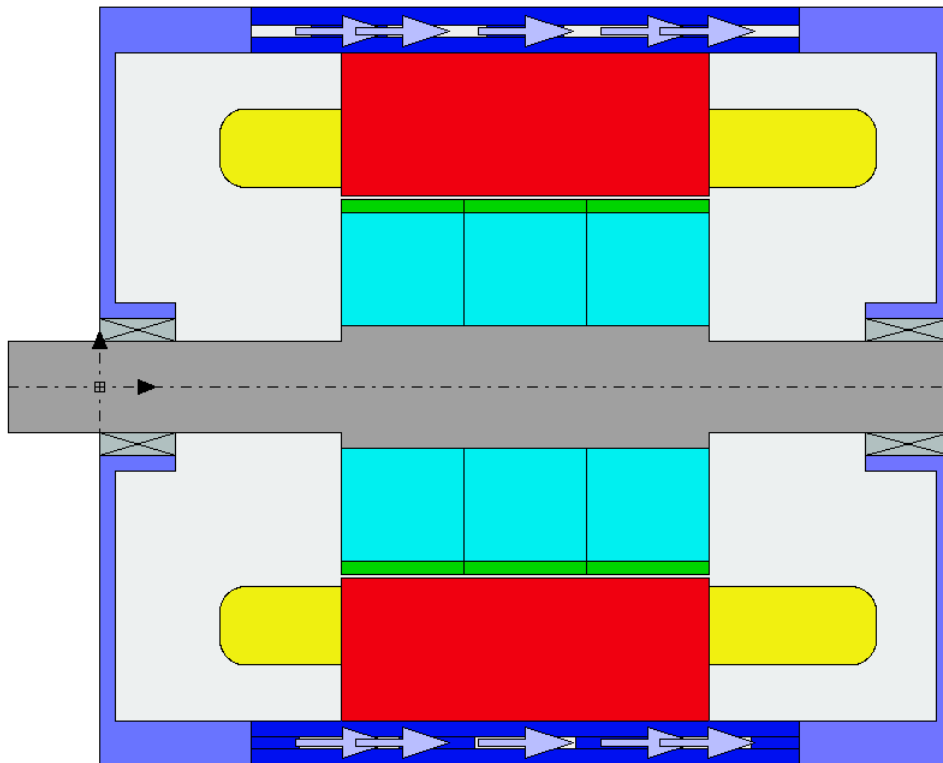


Figure 6.5.1: Axial section of the reviewed cooling jacket

graph the prefixed characteristics are satisfied as it is confirmed by the thermal trend.

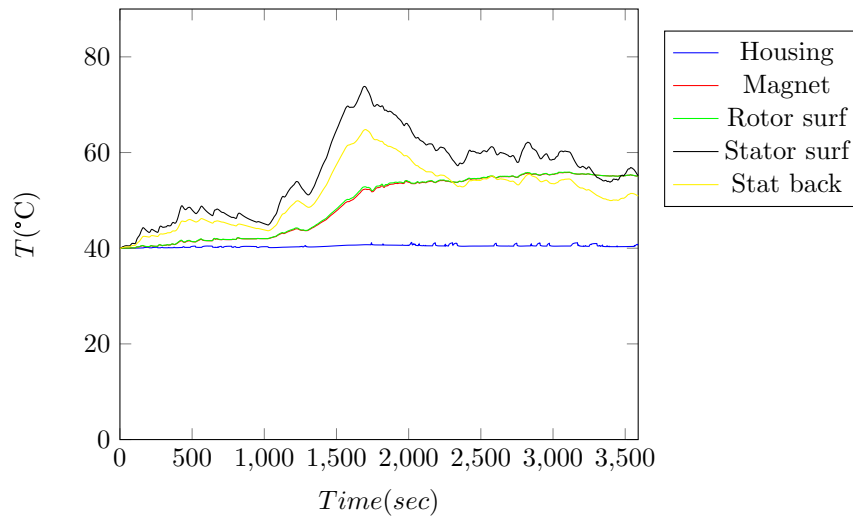


Figure 6.5.2: Temperature evolution in duty cycle thermal analysis with a redesigned cooling

# Chapter 7

## Conclusions

This thesis arises from the experimental requirement of analyzing a heavy-duty electric machine whose motors have been several times subjected to unexpected faults. Thus, the research aimed to find a method for continuous monitoring of a full electric vehicle equipped with a permanent magnet synchronous motor, by acquiring data with an electronic Arduino-based system connected to the vehicle CAN-Bus and by using them as input data for a reverse-engineered motor, which design has begun from the manufacturer's overall characteristics. This work fits the requirement of Industry 4.0, in which systems must be interconnected on a network, enabling real-time optimization and diagnostics. Data acquired were first analyzed through Matlab plots, which have shown an unbalanced thermal management. So an enhanced cooling jacket has been proposed to improve heat exchange considering both structural and thermal aspects. A method to analyze potentially critical working points and evaluate possible faults has been developed. Thermo-magnetic coupled FEM simulations have made possible the detection of failures or critical issues and finally have allowed the calculation of a safety factor, which states the distance from a fault condition.

In this work the existence of a retaining sleeve structure, useful to withstand the high centrifugal forces generated during high-speed functioning, was neglected. Moreover, the high number of degrees of freedom encountered during the design stage of the electric motor, has made difficult the preliminary design, for this reason it has been necessary the use of mathematical proportionality equations to determine the main geometrical ratios. A quantitative discussion on the losses has revealed the importance of the right choice of materials, disclosing also the different ways adopted by manufacturers and their effects on the rotor structures. The analysis of data from the electronic platform, have shown a motor particularly responsive to heat with sudden rises in temperature, which behaviour was considered dependent on an underestimation of heat exchange characteristic parameters, so it has been considered worthwhile the proposal of improvements to improve subsequent models. Considering the aforementioned thermal situation, a particular attention on demagnetization as possible faults due to operating conditions, has pointed out that any critical scenario occurs within the cycle recorded. However, nothing can be stated about a continuous operation, since the *Safety Coefficient* found and the curves reported highlight the close dependency on the temperature.

The future research will focus on innovative cooling solutions, regarding either the stator

inner regions and for the rotor, which installation wouldn't affect the correct motor functioning due to its faults, but allowing more powerful designs. Moreover, finding materials with minor losses can expand the high efficiency working range, reducing heat generated and power consumption. Another field of research is to investigate the rotor dynamic behaviour when it is mounted on a transmission axle, coupling the architecture modal analysis with advanced rotor structures. Further improvements may regard the implementation of a similar technique as a standard analysis for IoT remote control, allowing fault prediction and helping the service in failures detection.

# Bibliography of images

- [3] Edutecnica. *Dc motors*. URL: <https://www.edutecnica.it/apps/dcmotor/dcmotor.htm>.
- [5] ePaddock. *Motor*. URL: <https://www.epaddock.it/en/the-motor-for-the-motoe/>.
- [8] Oemer. *AC Synchronous reluctance motors*. Presentation.

# Bibliography of articles

- [1] H. Ahuett-Garza and T. Kurfess. “A brief discussion on the trends of habilitating technologies for Industry 4.0 and Smart manufacturing”. In: *Manufacturing Letters* 15 (2018). Industry 4.0 and Smart Manufacturing, pp. 60–63. ISSN: 2213-8463. DOI: <https://doi.org/10.1016/j.mfglet.2018.02.011>. URL: <https://www.sciencedirect.com/science/article/pii/S2213846318300270>.
- [2] Ali M. Bazzi. “Electric machines and energy storage technologies in EVs and HEVs for over a century”. In: *2013 International Electric Machines Drives Conference* (2013).
- [4] J. Xu; F. Wang; J. Feng; J. Xu. “Flux-weakening control of permanent magnet synchronous motor with direct torque control consideration variation of parameters”. In: *30th Annual Conference of IEEE Industrial Electronics Society, 2004. IECON 2004* (2004).
- [6] T. Han; Yun-C. Wang; Xue-F. Qin; Jian-X. Shen. “Investigation of Various Rotor Retaining Sleeve Structures in High-Speed PM Brushless Motors”. In: *21st International Conference on Electrical Machines and Systems (ICEMS)* (2018).
- [7] G. Vijay Kumar; C.-Hsiang Chuang; Min-Ze Lu; C.-Ming Liaw. “Development of an Electric Vehicle Synchronous Reluctance Motor Drive”. In: *IEEE Transactions on Vehicular Technology* (2020).
- [9] F. Mocera; A. Somà. “A Review of Hybrid Electric Architectures in Construction, Handling and Agriculture Machines”. In: *Intechopen* (Aug. 2021). DOI: 10.5772/intechopen.99132.
- [10] Mocera F.; Somà A. “Analysis of a parallel hybrid electric tractor for agricultural applications”. In: *Energies* 13 (2020), p. 3055.
- [11] Mocera F.; Somà A.; Clerici D. “Study of aging mechanisms in lithium-ion batteries for working vehicle applications”. In: *Fifteenth International Conference on Ecological Vehicles and Renewable Energies (EVER)* (2020).
- [12] Bimal K. Bose. “Power electronics and motor drives recent progress and perspective”. In: *IEEE Transactions on Industrial Electronics* 56 (Feb. 2008), pp. 581–588.
- [13] Dakshina M. Bellur; Marian K. Kazimierczuk. “DC-DC converters for electric vehicle applications”. In: *Electrical Insulation Conference and Electrical Manufacturing* (2007), pp. 286–293.
- [14] Xin-Qing Sheng; Wei Song. “Essentials of computational electromagnetics”. In: *Wiley-IEEE Press* (2012).

- [15] Dr. Duane Hanselman. *Brushless permanent magnet motor design*. Magna Physics Publishing.
- [16] J.C. Urresty; J.-Roger Riba; L. Romeral; A. G. G. Espinosa. “A Simple 2-D Finite-Element Geometry for Analyzing Surface-Mounted Synchronous Machines With Skewed Rotor Magnets”. In: *IEEE Transactions on Magnetics* (2010).
- [17] Fei Lin; K. T. Chau; C. C. Chan; Liu Chunhua. “Fault Diagnosis of Power Components in Electric Vehicles”. In: *Journal of Asian Electric Vehicles* (2013).
- [18] Lingyu Gao; Lubin Zeng; Jiaxin Yang; Ruilin Pei. “Application of grain-oriented electrical steel used in super-high speed electric machines”. In: *AIP Advances* (2020).
- [19] Puvan Arumugam; Zeyuan Xu; Antonino La Rocca; et Al. “High-Speed Solid Rotor Permanent Magnet Machines: Concept and Design”. In: *IEEE Transactions on Transportation Electrification* (2016).
- [20] Marcin Lefik; Krzysztof Komezka; Ewa Napieralska-Juszczak; Daniel Roger; Piotr Andrzej Napieralski. “Comparison of the reluctance laminated and solid rotor synchronous machine operating at high temperatures”. In: *COMPEL - The international journal for computation and mathematics in electrical and electronic engineering* (2019).
- [21] E. Vergori; F. Mocera; A. Somà. “Battery Modelling and Simulation Using a Programmable Testing Equipment”. In: *9th Computer Science and Electronic Engineering (CEECE)* (2017).
- [22] K. Ismail; Aam Muharam; M. Pratama. “Design of CAN Bus for Research Applications Purpose Hybrid Electric Vehicle Using ARM Microcontroller”. In: *2nd International Conference on Sustainable Energy Engineering and Application (ICSEEA) 2014 Sustainable Energy for Green Mobility* (2014).
- [23] F. Mocera; A. Somà. “Working Cycle requirements for an electrified architecture of a vertical feed mixer vehicle”. In: *AIAS 2018 International Conference on Stress Analysis* (2018).
- [24] Björn Sonnerud; Tord Bengtsson; Jörgen Blennow; Stanislaw M. Gubanski. “Dielectric heating in insulating materials subjected to voltage waveforms with high harmonic content”. In: *IEEE Transactions on Dielectrics and Electrical Insulation* 16.4 (2009).
- [25] J. Gonder; T. Markel; A. Simpson; M. Thornton. “Using GPS Travel Data to Assess the Real World Driving Energy Use of Plug-In Hybrid Electric Vehicles (PHEVs)”. In: *Transportation Research Board (TRB) 86th Annual Meeting* (2007).
- [26] F. Mocera; E. Vergori; A. Somà. “Battery Performance Analysis for Working Vehicle Applications”. In: *IEEE Transactions on Industry Applications* 56.1 (Jan. 2020), pp. 644–653.
- [27] F. Zhou; J. Shen; W. Fei; R. Lin. “Study of Retaining Sleeve and Conductive Shield and Their Influence on Rotor Loss in High-Speed PM BLDC Motors”. In: *IEEE Transactions on Magnetics* 42.10 (2006), pp. 3398–3400.
- [28] M.C. Ruzicka. “On dimensionless numbers”. In: *Chemical Engineering Research and Design* 86.8 (2008), pp. 835–868. ISSN: 0263-8762. DOI: <https://doi.org/10.1016/j.cherd.2008.03.007>. URL: <https://www.sciencedirect.com/science/article/pii/S0263876208000725>.

- [29] Kea-Ho Lee; Hyun-Rok Cha; Young-Bae Kim. “Development of an interior permanent magnet motor through rotor cooling for electric vehicles”. In: *Applied Thermal Engineering* 95 (2016), pp. 348–356. ISSN: 1359-4311.
- [30] Junkui Huang; Shervin Shoai Naini; Richard Miller; Denise Rizzo. “A Hybrid Electric Vehicle Motor Cooling System– Design, Model, and Control”. In: *IEEE Transactions on Vehicular Technology* (2019).
- [31] Mariusz Baranski, Wojciech Szelag, and Wieslaw Lyskawinski. “Analysis of the Partial Demagnetization Process of Magnets in a Line Start Permanent Magnet Synchronous Motor”. In: *Energies* 13.21 (2020). ISSN: 1996-1073. DOI: 10.3390/en13215562. URL: <https://www.mdpi.com/1996-1073/13/21/5562>.
- [32] Dmitry Egorov; Ilya Petrov; J. Pyrhönen; et Al. “Linear recoil curve demagnetization models for ferrite magnets in rotating machinery”. In: *IECON 2017 - 43rd Annual Conference of the IEEE Industrial Electronics Society* 2046-2052 (2017).
- [33] Stefan Sjökvist. “Demagnetization Studies on Permanent Magnets”. In: *Uppsala Universitet* (2014).